



Quantitative decoding of coupled carbon and energy metabolism in *Pseudomonas putida* for lignin carbon utilization



Nanqing Zhou¹, Rebecca A. Wilkes², Xinyu Chen¹, Kelly P. Teitel¹, James A. Belgrave³, Gregg T. Beckham², Allison Z. Werner², Yanbao Yu⁴ & Ludmilla Aristilde^{1,3}

Soil *Pseudomonas* species, which thrive on lignin derivatives, are widely explored for biotechnology applications in lignin valorization. However, how the native metabolism coordinates phenolic carbon processing with required cofactor generation remains poorly understood. Here, we achieve quantitative understanding of this metabolic balance through a detailed multi-omics investigation of *Pseudomonas putida* KT2440 grown on four common phenolic acid substrates: ferulate, *p*-coumarate, vanillate, and 4-hydroxybenzoate. Relative to succinate, proteomics reveals > 140-fold increase in transport and catabolic proteins for aromatics, but metabolomics identifies bottlenecks in initial catabolism to maintain favorable cellular energy charge, which is compromised in mutants with resolved bottlenecks. Up to 30-fold increase in pyruvate carboxylase and glyoxylate shunt proteins implies a metabolic remodeling confirmed by kinetic ¹³C-metabolomics. Quantitative analysis by ¹³C-fluxomics demonstrates coupling of this remodeling with cofactor production. Specifically, anaplerotic carbon recycling through pyruvate carboxylase promotes tricarboxylic acid cycle fluxes to generate 50–60% NADPH yield and 60–80% NADH yield, resulting in up to 6-fold greater ATP surplus than with succinate metabolism; the glyoxylate shunt sustains cataplerotic flux through malic enzyme for the remaining NADPH yield. This quantitative blueprint affords cofactor imbalance predictions in proposed engineering of key metabolic nodes in lignin valorization pathways.

Lignin, a structural polymer in plant biomass that is considered the second most abundant biopolymer after cellulose, represents an important renewable carbon source¹. Chemical depolymerization of lignin generates various phenolic acid compounds, which can be used as feedstocks for bioproduction of valuable chemicals^{2–4}. These lignin-related phenolic acid structures include hydroxybenzoates (4-hydroxybenzoate, vanillate, gallate, and syringate) and hydroxycinnamates (*p*-coumarate and ferulate)⁵. Soil *Pseudomonas* species have native metabolic capabilities to process benzoate, 4-hydroxybenzoate (4HB), vanillate (VAN), gallate, *p*-coumarate (COU), and ferulate (FER)⁶. Of particular interest is *Pseudomonas putida* KT2440, which is extensively explored as a chassis for biotechnology^{7–11}, including notably the bioconversion of lignin-derived aromatics^{12,13}. Encoded in *P. putida* KT2440 are pathways for the catabolism of hydroxybenzoates and hydroxycinnamates involving *ortho*-cleavage of the intermediate

protocatechuate (PCA) through β-ketoadipate to generate carbon influx into the tricarboxylic acid (TCA) cycle in the central carbon metabolism⁶ (Fig. 1A). In the peripheral pathways upstream of β-ketoadipate, the uptake and catabolism of hydroxycinnamates (COU and FER) and hydroxybenzoates (4HB and VAN) to PCA are catalyzed by a series of enzymes with distinct cofactor specificities^{6,13–17} (Fig. 1A). Previous metabolic engineering of *P. putida* targeted directing carbon influx from phenolic carbons from initial catabolism towards desired products such as PCA, vanillin, β-ketoadipate, muconic acid, pyridine 2,4-dicarboxylic acid, adipic acid, indigoidine, free fatty acids and polyhydroxyalkanoates^{18–31}. Metabolic bottlenecks, which were inferred from extracellular accumulation of VAN in FER-fed cells or of 4HB in COU-fed cells^{21,29,30,32–34}, could not be overcome completely via genetic engineering due to cofactor deficiency^{21,30,32}. Therefore, metabolic engineering to enhance phenolic carbon conversion must address

¹Department of Civil and Environmental Engineering, McCormick School of Engineering and Applied Science, Northwestern University, Evanston, IL, USA.

²Renewable Resources and Enabling Sciences Center, National Renewable Energy Laboratory, Golden, CO, USA. ³Northwestern Center for Synthetic Biology, Northwestern University, Evanston, IL, USA. ⁴Department of Chemistry and Biochemistry, University of Delaware, Newark, DE, USA.

e-mail: ludmilla.aristilde@northwestern.edu

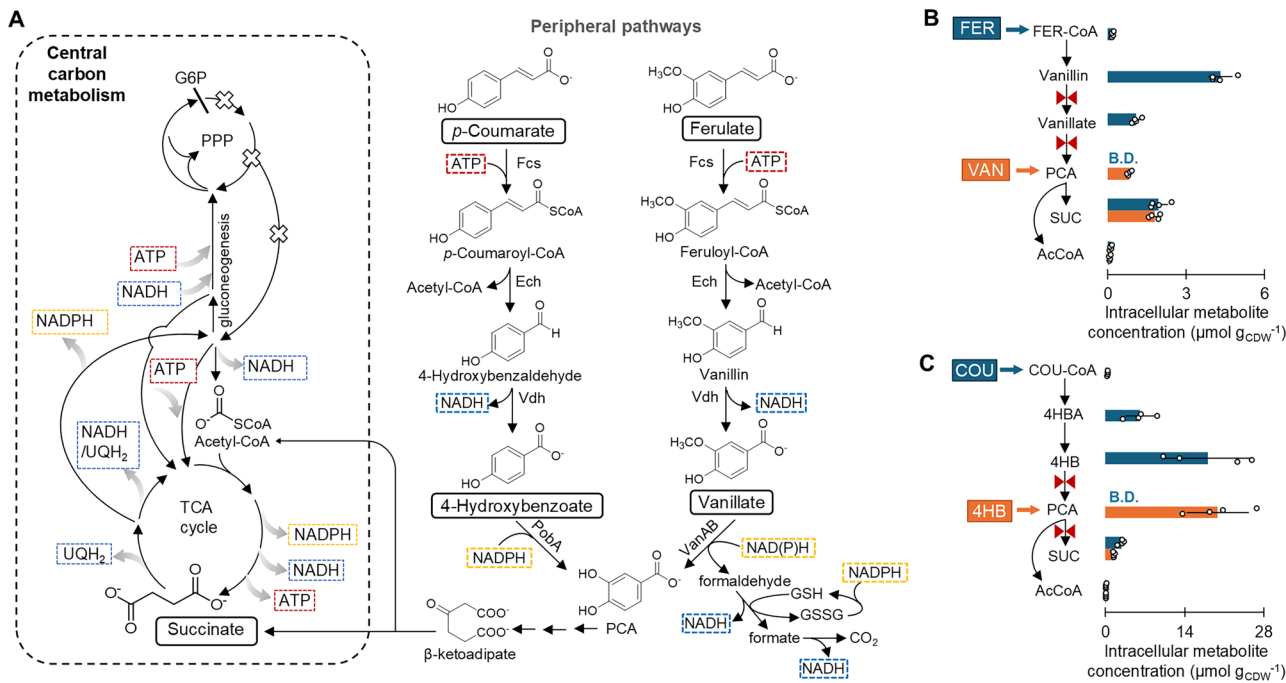


Fig. 1 | Intracellular evidence of bottleneck nodes in initial catabolic pathways of phenolic acid substrates. A Schematic illustration of cofactor investment and production in the peripheral pathway and central carbon metabolism.

B Intracellular levels of metabolites involved in FER and VAN utilization in the coniferyl branch; the colored arrows indicate the catabolic entry of the different substrates, blue arrow for FER and orange arrow for VAN. **C** Intracellular levels of intermediates involved in COU and 4HB utilization; the colored arrows indicate the catabolic entry of the different substrates, blue arrow for COU and orange arrow for 4HB. In A, the white crosses are to represent the reported lack of carbon flux through

the oxPPP and Entner–Doudoroff pathway during gluconeogenic substrate metabolism⁴⁸; the oxPPP reactions⁹¹ were therefore not involved in cofactor production during the metabolism of the phenolic acids. Only NADH was reported to be produced during formaldehyde and formate oxidation based on previous studies^{92,93}. In B, C red bowties indicate the identified bottlenecks. B.D. below detection limit. FER ferulate, FER-CoA feruloyl-CoA, COU *p*-coumarate, COU-CoA *p*-coumaroyl-CoA, GSH glutathione, GSSG glutathione disulfide. Data in (B, C) are shown as mean ± standard deviation of four independent biological replicates ($n = 4$).

appropriate cofactor supply. However, largely lacking is a quantitative understanding of how the native metabolic network in *P. putida* KT2440 couples carbon fluxes from phenolic acid structures with required cofactor production.

Metabolic flux modeling or fluxomics constrained by ¹³C-metabolomics data provides quantitative analysis of carbon fluxes^{35–40}. Previous ¹³C-fluxomics studies of *P. putida* focused on glycolytic metabolism for sugars (i.e., glucose, xylose) or gluconeogenic metabolism for succinate (SUC)^{41–51}. The only two fluxomics studies of aromatic carbon metabolism in *P. putida*, for benzoate alone or with glucose as a co-substrate^{41,52}, both illustrated the activation of the glyoxylate shunt, which conserved carbon by channeling isocitrate away from the canonical decarboxylation steps in the TCA cycle. Flux through the glyoxylate shunt can feed into malic enzyme for NADPH generation, or malate dehydrogenase, for NADH or ubiquinol generation. Interestingly, for benzoate catabolism, the flux through malate dehydrogenase was either 3-fold higher than the flux through malic enzyme or there was only flux through malate dehydrogenase, both of which would be advantageous to satisfy the NADH demand for benzoate catabolism through the catechol pathway in *P. putida*^{41,52}. For the catabolism of hydroxybenzoate and hydroxycinnamate structures, which is funneled through PCA instead of catechol, it remains unknown how metabolic fluxes would be partitioned in *P. putida* to optimize the catabolic pathways with cofactor supply (Fig. 1A).

While ATP in aerobic bacteria is generated primarily through oxidative phosphorylation of NADH produced in glycolysis and the TCA cycle⁵³, the supply of NADPH required for biosynthesis and stress tolerance is produced from different metabolic routes. During growth on glucose, NADPH production in *P. putida* includes the important involvement of glucose-6-phosphate dehydrogenase and 6-phosphogluconate dehydrogenase in the oxidative pentose phosphate pathway (oxPPP)^{44,47}. However, minimal to no

flux through oxPPP was reported during growth on two gluconeogenic substrates (SUC or benzoate)^{48,52}. Instead, gluconeogenic metabolism in *P. putida* was reported to rely on high flux through isocitrate dehydrogenase and malic enzyme in the TCA cycle to produce NADPH, and on transhydrogenase reactions to generate NADPH from excess NADH pool⁴⁸. Whether *P. putida* would rely on similar metabolic routing or energetic bypass for NADPH production during phenolic acid utilization remains to be elucidated.

The cataplerotic and anaplerotic nodes, which distribute respectively carbon fluxes from the TCA cycle to gluconeogenesis and from lower glycolysis to the TCA cycle⁵⁴, have implications for cofactor balance (Fig. 1A). In the cataplerotic direction, due to lack of phosphoenolpyruvate (PEP) carboxykinase for the decarboxylation of oxaloacetate (OAA) to PEP⁵⁵, *P. putida* KT2440 must rely on either malic enzyme to convert malate to pyruvate with NADPH production or OAA decarboxylase to convert OAA to pyruvate with no cofactor involved⁵⁶. In the anaplerotic direction, pyruvate carboxylation to OAA consumes ATP, while PEP carboxylation to OAA has no cofactor input⁵⁶. It remains unclear how *P. putida* KT2440 would distribute carbon fluxes between cataplerosis and anaplerosis to meet the demand for reducing equivalents and energy required for phenolic carbon catabolism.

Here, our central hypothesis was that remodeling of metabolic nodes into and within the TCA cycle by *P. putida* KT2440 would establish the fluxes of NAD(P)H and ATP to satisfy the cofactor demands in the *p*-coumaroyl and coniferyl pathways (Fig. 1A). We tested our hypothesis by employing genetic engineering, metabolomics profiling, whole-cell proteomics, kinetic ¹³C-metabolomics, and ¹³C-fluxomics during feeding of *P. putida* KT2440 on FER, COU, VAN, or 4HB as the sole carbon source, compared to SUC as non-aromatic substrate reference. First, using quantitative metabolomics for cofactor profiling in wild-type and mutant strains,

we investigated how the cellular energy state would be influenced by alterations in the aromatic carbon influx due to overexpression of key bottleneck-relevant genes. Second, to elucidate the metabolic network that underlies the cellular energy state, we profiled protein levels to identify metabolic remodeling nodes and verify these nodes using kinetic ¹³C-profiling in metabolites coupled with ¹³C-carbon mapping. Third, we integrated the proteomics and ¹³C-metabolomics data to perform ¹³C-fluxomics to map quantitatively carbon fluxes throughout the metabolic network. Fourth, we leveraged the quantitative flux analysis to determine production and consumption rates of cofactors and evaluate metabolic flux controls on cofactor maintenance during conversion of the different lignin-derived phenolic acid compounds. This research provides the first quantitative mapping of the relationship between carbon metabolism and energy metabolism in *P. putida* KT2440 utilizing different hydroxycinnamate and hydroxybenzoate substrates, thereby guiding the predictions of cofactor balancing required during engineering of metabolic pathways for lignin valorization.

Results

Favorable cellular energy balance is sustained despite bottleneck nodes in native catabolism

Bottlenecks were proposed previously at three nodes in initial phenolic acid catabolism, based on extracellular metabolic overflow in exponentially growing cells: the VanAB node in the coniferyl branch^{21,29}, the PobA node in the *p*-coumaroyl branch^{21,30,32}, and the PcaHG node downstream of both branches²⁹ (Fig. 1A). Here, we obtained direct evidence using intracellular metabolomics analysis and ¹³C kinetic isotopic profiling of exponentially growing cells to confirm the three reported bottlenecks (at VanAB, PobA, and PcaHG nodes) and identify one additional bottleneck at the Vdh node (Fig. 1B, C; Supplementary Information (SI), Fig. S1).

In the coniferyl branch, bottleneck at the Vdh node was characterized by a 20-fold and 4-fold higher intracellular vanillin concentration ($4.3 \pm 0.5 \mu\text{mol g}_{\text{CDW}}^{-1}$) relative to its precursor feruloyl-CoA ($0.2 \pm 0.03 \mu\text{mol g}_{\text{CDW}}^{-1}$) and its downstream metabolite vanillate ($1.1 \pm 0.2 \mu\text{mol g}_{\text{CDW}}^{-1}$), respectively; further downstream, PCA was below the detection limit of $0.1 \mu\text{M}$ (Fig. 1B). This bottleneck was further illustrated by 50% lower incorporation of ¹³C-FER in vanillin compared to feruloyl-CoA within 1 min of isotope switch ($P < 0.05$) (SI, Fig. S1). Even with VAN as the direct carbon source, PCA level remained low ($0.8 \pm 0.1 \mu\text{mol g}_{\text{CDW}}^{-1}$), in accordance with inefficient VAN conversion to intracellular PCA by VanAB (Fig. 1B). In the *p*-coumaroyl branch, in line with the reported bottleneck node at PobA^{21,30,32}, there was a high intracellular 4HB level ($18.1 \pm 7.6 \mu\text{mol g}_{\text{CDW}}^{-1}$) during COU catabolism, while 4-hydroxybenzaldehyde (4HBA) level was 67% lower ($P < 0.05$) and PCA level was below the detection limit (Fig. 1C). Furthermore, consistent with this bottleneck at PobA, there was 31% smaller fraction of ¹³C-COU carbons in 4HB than in 4HBA within 1 min ($P < 0.01$) (SI, Fig. S1). During growth on 4HB, PCA accumulated ($19.8 \pm 5.4 \mu\text{mol g}_{\text{CDW}}^{-1}$), in accordance with the reported bottleneck at PcaHG (Fig. 1C)²⁹.

Towards resolving the bottlenecks in the coniferyl branch, we constructed four mutant strains: RW124 with *vanAB* overexpression, RW125 with combined overexpression of *vanAB* and *pcaHG*, RW127 with overexpression of *vdh*, and RW126 with stacked overexpression of *vdh*, *vanAB*, and *pcaHG* (Fig. 2A). Overexpression of *vdh* (strain RW127) led to an 80% decrease in vanillin and a 24-fold increase in VAN ($P < 0.001$), indicating that addressing the bottleneck at Vdh triggered a downstream bottleneck at VanAB (Fig. 2B). Compared to metabolite levels in RW127 fed on FER, a decreased VAN level (by 93%, $P < 0.001$) in RW126 indicated simultaneous alleviation of the bottlenecks at both Vdh and VanAB (Fig. 2B). Compared to the wild-type strain grown on VAN, the unchanged intracellular PCA level in RW124 and depletion of PCA (by 83%, $P < 0.001$) in RW125 demonstrated efficient PCA cleavage and thus elimination of the bottleneck at PcaHG during VAN catabolism (Fig. 2C). Cellular energy charge was 25–44% lower in the mutant strains in the coniferyl branch compared to the wild-type strain ($P < 0.05$) (Fig. 2B, C; SI, Table S1).

To resolve the bottlenecks in the *p*-coumaroyl branch, we prepared three mutant strains that overexpressed either *pobA* (RW128), *pcaHG* (RW123), or both *pobA* and *pcaHG* (RW129) (Fig. 2D). Compared to the wild-type strain, the bottlenecks were resolved in RW128 and RW123, characterized by a 90% decrease in 4HB during growth on COU and a 50% decrease in PCA during growth on 4HB ($P < 0.05$), respectively (Fig. 2E, F). Similar to the coniferyl branch, the energy charge of the mutants of the *p*-coumaroyl branch was 32–40% lower than in the wild-type stain ($P < 0.05$) (Fig. 2E, F; SI and Table S1).

In sum, alleviation of native metabolite buildups in initial substrate catabolism led to adverse change in the cellular energy charge, thereby implying an interplay between the regulation of phenolic carbon influx and cofactor balance and a potential energy burden caused by gene overexpression⁵⁰. It remains to be investigated whether this metabolic burden could be overcome through alternative genetic engineering approaches, such as tuning of the ribosomal binding site or chromosomal integration. Interestingly, when we compared growth phenotypes of the *P. putida* KT2440 cells on FER, COU, VAN, or 4HB to reported growth phenotype on SUC (a nonaromatic substrate ref. 48), the biomass yield of *P. putida* was similar across all five substrates ($P = 0.64$ –0.99), despite the differences in growth and substrate depletion rates (SI, Fig. S2). However, we obtained 25–31% higher energy charge when the wild-type cells were grown on the phenolic substrates compared to growth on SUC ($P < 0.001$) (SI, Fig. S2). These data further implied that carbon influx during phenolic acid assimilation was optimized for a favorable cellular energy charge. Towards understanding the metabolic mechanisms underlying native cofactor balance, we investigated protein levels, metabolite pools, and the network of carbon fluxes during processing of the different phenolic acid compounds.

Abundances of transporters and specialized enzymes are modulated to adapt to phenolic carbon influx

We obtained whole-cell proteomics data to compare the abundance of proteins involved in membrane transport, the coniferyl branch, the *p*-coumaroyl branch, and the central carbon metabolism in *P. putida* cells fed on each phenolic substrate relative to cells fed on SUC (Fig. 3). For each of the four biological replicates across the five growth substrates, we employed a high-resolution proteomics method to capture over 4300 proteins out of the 5950 total proteins encoded by *P. putida* KT2440, including low-abundance proteins that are typically undetected (SI, Table S2). In agreement with the assignment of HcnK as the common transporter for hydroxycinnamate uptake to both the coniferyl and *p*-coumaroyl branches¹³, abundance of HcnK was 700-fold greater in *P. putida* cells fed with FER or COU relative to SUC (Fig. 3A; SI, Table S3). The HcnK abundance was also 9-fold to 13-fold higher in cells grown on VAN and 4HB relative to SUC (Fig. 3A; SI, Table S3), indicating that the abundance of this transporter was also induced by downstream metabolites in the pathways. For the VAN transporter VanK¹³, its abundance was 830-fold higher in cells fed with VAN or FER compared to SUC (Fig. 3A; SI, Table S3), consistent with the dependence of VanK level on the presence of VAN either as a substrate or as an intermediate in FER catabolism (Fig. 1A). Similarly, the abundance of the 4HB transporter PcaK was increased to similar extent (>140-fold) during growth across all four phenolic substrates compared to growth on SUC, in accordance with PcaK serving also as a transporter of PCA^{13,16}, a common downstream intermediate in both the coniferyl and *p*-coumaroyl branches (Fig. 3A; SI, Table S3).

After substrate uptake, a series of cofactor-dependent enzymes are involved in the initial catabolism (Fig. 3A). Compared to SUC-fed cells, the abundances of Fcs, Ech, and Vdh, which collectively catalyze the conversion of FER to VAN or COU to 4HB, were up to 590-fold higher in cells fed on FER or COU, but remained unchanged in cells grown on VAN or 4HB (Fig. 3A; SI, Table S3). The abundance of VanAB, which catalyzes O-demethylation of VAN to produce PCA and formaldehyde, was up to 2700-fold higher in cells grown on FER or VAN compared to SUC; the corresponding increase during feeding on COU and 4HB was 60-fold (Fig. 3A;

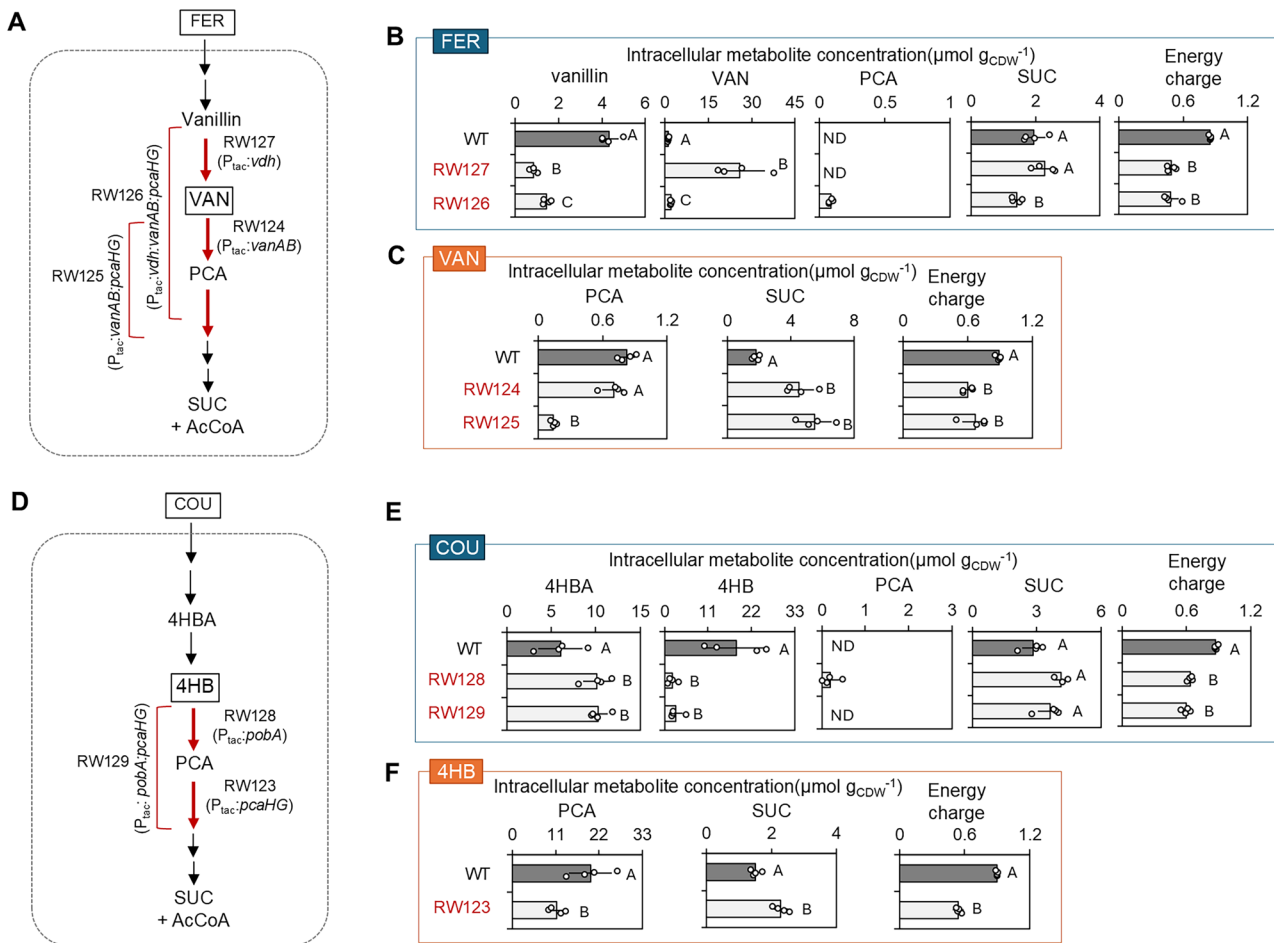


Fig. 2 | Resolved bottleneck nodes in initial catabolism and unfavorable cellular energy state indicated by decreased energy charge values. **A** Targeted nodes in the coniferyl branch for gene overexpression. Intracellular metabolite levels and energy charge in the wild-type and mutant strains during feeding on **B** FER and **C** VAN. **D** Targeted nodes in the *p*-coumaroyl branch for gene overexpression. Intracellular metabolite levels and energy charge in the wild-type and mutant strains during

feeding on **E** COU and **F** 4HB. FER-CoA feruloyl-CoA, COU-CoA *p*-coumaroyl-CoA. In **B**, **C**, and **E**, one-way ANOVA was performed followed by Tukey's HSD post hoc test to determine the significance. In **F**, unpaired *t*-test was performed to evaluate the significance. Statistically significant differences ($P < 0.05$) are denoted by a change in letter. Data in **B**, **C**, **E**, and **F** are shown as mean \pm standard deviation of four independent biological replicates ($n = 4$).

SI, Table S3). To avoid the accumulation of toxic formaldehyde, *P. putida* can oxidize formaldehyde to CO_2 via formate as an intermediate using formaldehyde dehydrogenase (FrmA, FdhA) and formate dehydrogenase (Fdh, Fmd, Fdo) (Fig. 3B; SI, Table S3)⁵⁷. Accordingly, relative to SUC-grown cells, the abundance of FrmA and FdhD was up to 40-fold higher in cells grown on FER or VAN, but remained unchanged in cells grown on COU or 4HB (Fig. 3B; SI and Table S3). Related to stress tolerance strategies^{58,59}, abundance of TtgABC efflux pump was 3-fold higher in VAN-grown cells compared to SUC-fed cells (SI, Table S3), suggesting its involvement in formaldehyde tolerance. For the conversion of 4HB to PCA, the abundance of PobA was up to 3100-fold higher during feeding on COU or 4HB relative to SUC feeding; the corresponding change was up to 550-fold higher in cells grown on FER or VAN (Fig. 3A; SI, Table S3).

Taken together, the increased abundance of the initial catabolic enzymes across all substrates implied co-regulation in the utilization of the different phenolic acid substrates. In fact, compared to growth on SUC, the levels of enzymes (PcaHGBCDJIF) involved in the *ortho*-cleavage of PCA via the β -ketoadipate pathway showed 40-fold to 500-fold increase during growth on the four phenolic substrates (Fig. 3A; SI, Table S3). Importantly, the β -ketoadipate pathway generates SUC and acetyl-CoA as additional carbon influxes into the TCA cycle compared to metabolism of SUC alone (Fig. 3A). Next, we evaluated changes in protein abundances in the central carbon metabolism (Fig. 3C).

Fluxes through β -ketoadipate pathway and enhanced anaplerosis promote carbon retention in the TCA cycle

Only three nodes in central carbon metabolism showed greater than 2-fold changes in protein abundances during growth on the phenolic substrates relative to growth on SUC. First, we observed 2.5-fold to 6-fold more abundant pyruvate carboxylase (Pyc), which catalyzes the anaplerotic reaction of pyruvate carboxylation to OAA, while there was little to no change (<2-fold) in the abundance of phosphoenolpyruvate carboxylase (Ppc), which catalyzes the other anaplerotic reaction of PEP carboxylation, suggesting a dominant role of Pyc during growth on the phenolic acid compounds (Fig. 3C; SI, Table S3). Second, the two enzymes (AceA and GlcB) involved in the glyoxylate shunt were 2-fold to 30-fold more abundant (Fig. 3C; SI, Table S3). Third, the abundance of AceE and AceF, which catalyze pyruvate to acetyl-CoA, was up to 6-fold lower in cells fed on FER or COU, potentially due to the additional influx of acetyl-CoA from the hydroxycinnamate substrates. To corroborate the metabolic remodeling inferred from the proteomics data, we performed kinetic ^{13}C -profiling of *P. putida* KT2440 cells switched from unlabeled substrates to 50% phenyl- $^{13}\text{C}_6$ -FER, phenyl- $^{13}\text{C}_6$ -COU, phenyl- $^{13}\text{C}_6$ -VAN, phenyl- $^{13}\text{C}_6$ -4HB, or U $^{13}\text{C}_4$ -SUC (Fig. 4A).

The kinetic ^{13}C -profiling of intracellular metabolites captured the assimilation of substrate carbons in specific metabolic pathways. The slower incorporation of ^{13}C into the coniferyl branch relative to the *p*-coumaroyl

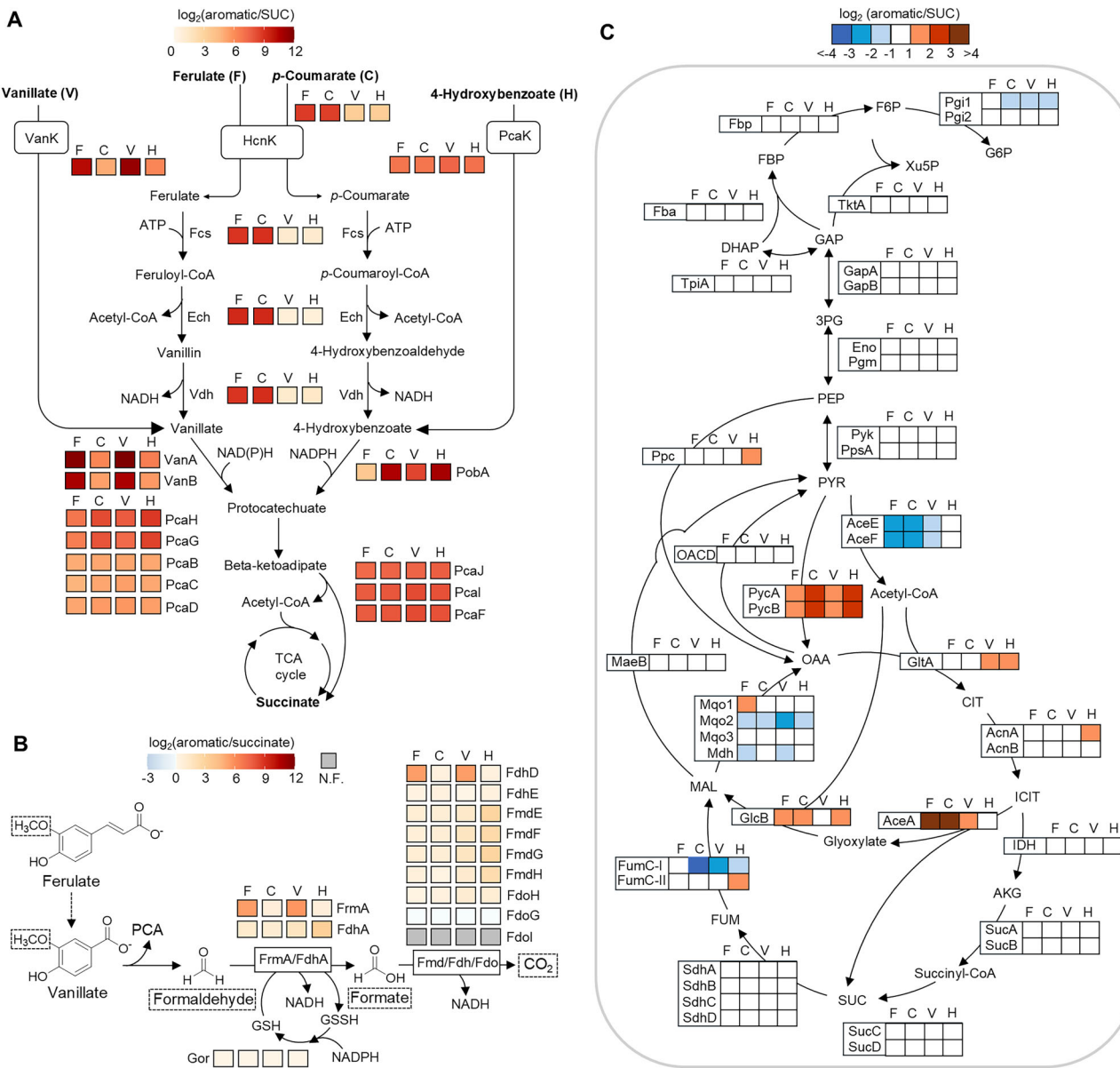


Fig. 3 | Co-regulation of initial catabolism and selective remodeling nodes in central carbon metabolism. Log₂ fold change in protein abundance in A the peripheral pathways, B formaldehyde oxidation pathway, and C central carbon metabolism during feeding on each phenolic acid substrate compared to SUC. In B, Only NADH was reported to be produced during formaldehyde and formate oxidation based on previous studies^{92,93}. HcnK hydroxycinnamic acid transporter, VanK vanillate transporter, PcaK 4-hydroxybenzoate/protocatechuate transporter, Fcs feruloyl-CoA synthase, Ech feruloyl-CoA hydratase-lyase, Vdh vanillin dehydrogenase, VanAB vanillate O-demethylase, PobA 4-hydroxybenzoate 3-monooxygenase, PcaH protocatechuate 3,4-dioxygenase beta chain, PcaG protocatechuate 3,4-dioxygenase alpha chain, PcaC 4-carboxymuconolactone decarboxylase, PcaB 3-carboxy-cis,cis-muconate cycloisomerase, PcaD 3-oxoadipate enol-lactonase, PcaIJ 3-oxoadipate CoA-transferase, PcaF betaketoadipyl-CoA thiolase, FrmA formaldehyde dehydrogenase, FdhA formaldehyde dehydrogenase, FmdEFGH formate dehydrogenase, FdhDE formate dehydrogenase, FdoHGI formate dehydrogenase, Gor glutathione reductase, Fbp fructose-1,6-bisphosphatase, Pgi glucose-6-phosphate isomerase, Fba fructose-1,6-bisphosphate aldolase, TktA transketolase, TpiA triosephosphate isomerase, Gap glyceraldehyde-3-phosphate dehydrogenase, Eno enolase, Pgm phosphoglucomutase, Pyk pyruvate kinase, PpsA phosphoenolpyruvate synthase, Ppc phosphoenolpyruvate carboxylase, OACD oxaloacetate decarboxylase, AceEF pyruvate dehydrogenase, PycAB Pyruvate carboxylase, MaeB malic enzyme, GltA citrate synthase, Acn aconitase hydratase, IDH isocitrate dehydrogenase, SucAB oxoglutarate dehydrogenase, SucCD succinyl-CoA ligase, FumC fumarate hydratase, Mqd malate:quinone oxidoreductase, Mdh malate dehydrogenase, AceA isocitrate lyase, GlcB malate synthase. Metabolite abbreviations: G6P glucose-6-phosphate, F6P fructose-6-phosphate, FBP fructose-1,6-bisphosphate, Xu5P xylose-5-phosphate, GAP glyceraldehyde-3-phosphate, DHAP dihydroxyacetone phosphate, 3PG 3-phosphoglycerate, PEP phosphoenolpyruvate, PYR pyruvate, CIT citrate, ICIT isocitrate, AKG alpha-ketoglutarate, FUM fumarate, MAL malate, OAA oxaloacetate. Only NADH is produced during formaldehyde and formate oxidation based on previous studies^{92,93}. Data of the protein abundances and metabolite levels from four independent biological replicates ($n = 4$) are provided in SI, Tables S3 and S4. The full dataset of proteomics is provided in Supplementary Data 1.

transketolase, TpiA triosephosphate isomerase, Gap glyceraldehyde-3-phosphate dehydrogenase, Eno enolase, Pgm phosphoglucomutase, Pyk pyruvate kinase, PpsA phosphoenolpyruvate synthase, Ppc phosphoenolpyruvate carboxylase, OACD oxaloacetate decarboxylase, AceEF pyruvate dehydrogenase, PycAB Pyruvate carboxylase, MaeB malic enzyme, GltA citrate synthase, Acn aconitase hydratase, IDH isocitrate dehydrogenase, SucAB oxoglutarate dehydrogenase, SucCD succinyl-CoA ligase, FumC fumarate hydratase, Mqd malate:quinone oxidoreductase, Mdh malate dehydrogenase, AceA isocitrate lyase, GlcB malate synthase. Metabolite abbreviations: G6P glucose-6-phosphate, F6P fructose-6-phosphate, FBP fructose-1,6-bisphosphate, Xu5P xylose-5-phosphate, GAP glyceraldehyde-3-phosphate, DHAP dihydroxyacetone phosphate, 3PG 3-phosphoglycerate, PEP phosphoenolpyruvate, PYR pyruvate, CIT citrate, ICIT isocitrate, AKG alpha-ketoglutarate, FUM fumarate, MAL malate, OAA oxaloacetate. Only NADH is produced during formaldehyde and formate oxidation based on previous studies^{92,93}. Data of the protein abundances and metabolite levels from four independent biological replicates ($n = 4$) are provided in SI, Tables S3 and S4. The full dataset of proteomics is provided in Supplementary Data 1.

branch was consistent with up to 58% slower uptake rates of the respective substrates (SI, Figs. S1 and S2). After 1 min, the ¹³C-labeled fractions of the intracellular SUC were at up to 24% in cells grown on FER and VAN, but at up to 52% in cells grown on COU and 4HB ($P < 0.001$) (Fig. 4B). The

¹³C-labeled fraction of acetyl-CoA in cells grown on the hydroxycinnamates (FER and COU) was up to 50% lower than in cells grown on the hydroxybenzoates (VAN and 4HB) ($P < 0.05$), due to the production of unlabeled acetyl-CoA via Ech-mediated reaction on the hydroxycinnamates (Fig. 4B).

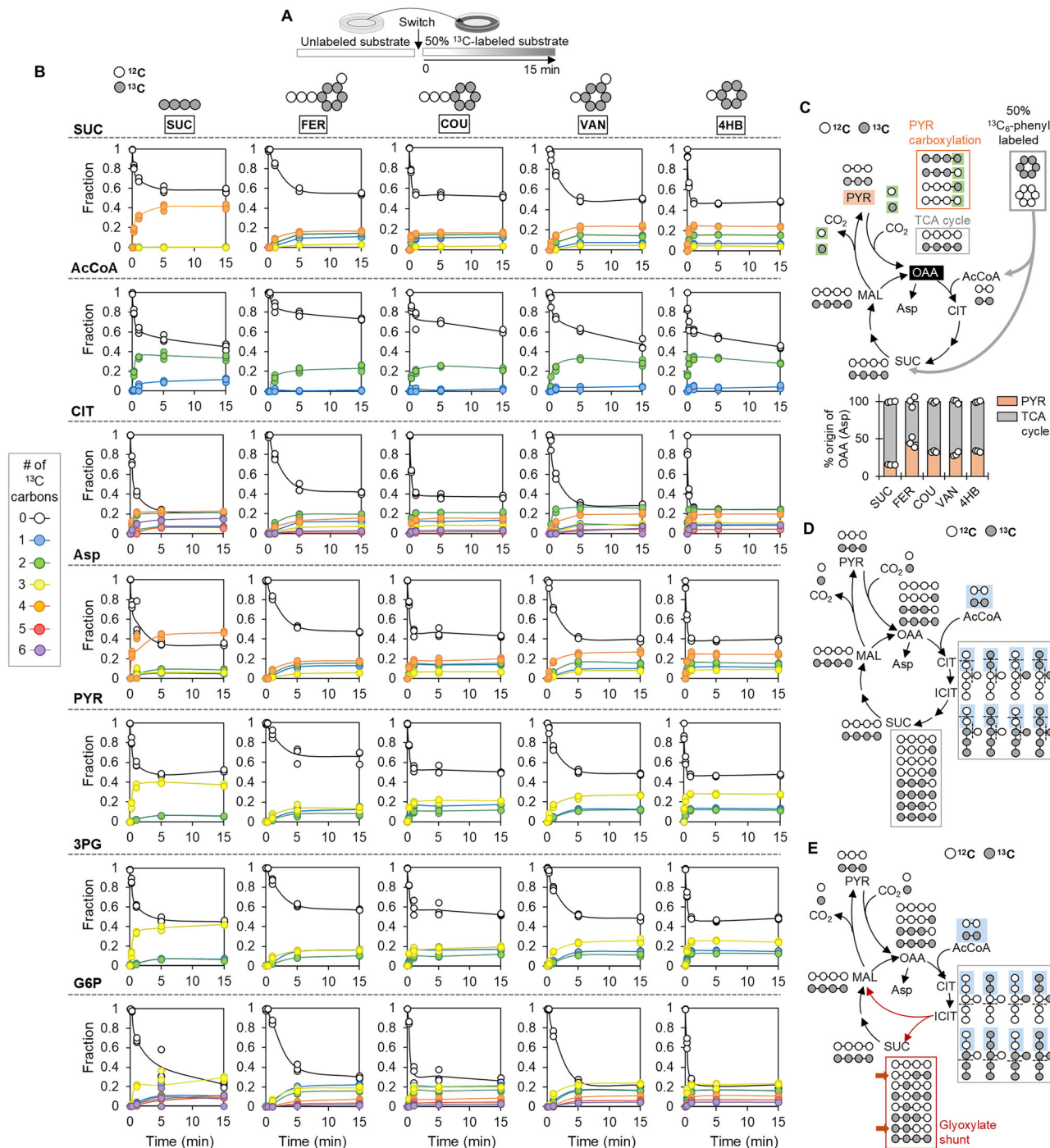


Fig. 4 | Kinetic ¹³C-profiling and carbon mapping of metabolic flux partitioning revealed metabolic remodeling nodes in the central carbon metabolism.

A Schematic illustration of kinetic isotope incorporation experiment using 50% ¹³C-labeled substrates. **B** Kinetic ¹³C-profiling of central carbon metabolites.

C Contribution from pyruvate versus malate to the oxaloacetate pool determined by carbon mapping when cells were grown on 50% ¹³C-labeled phenolic substrates or SUC. Isotopologues of TCA cycle intermediates predicted by carbon mapping when assuming **D** 100% canonical TCA cycle and **E** 100% glyoxylate shunt. Kinetic

¹³C-profiling of dihydroxyacetone phosphate, PEP, alpha-ketoglutarate, and sedoheptulose-7-phosphate are provided in SI, Fig. S5. We presented the data in **B** as individual data points in three independent biological replicates ($n = 3$), some of the data points are invisible due to the highly reproducibility among replicates. Values of individual data points for kinetic ¹³C-metabolomics are provided in Supplementary Data 2. Asp aspartate, other abbreviations of metabolites are the same as shown in Fig. 3.

Furthermore, consistent with the additional acetyl-CoA influx from the β -ketoadipate pathway, ¹³C-labeled acetyl-CoA was predominantly doubly ¹³C-labeled (>90%) during growth on the phenolic substrates (Fig. 4B). Despite similar substrate uptake rates, ¹³C-labeled fraction within 15 s was up to 2-fold higher in 4HB-grown cells ($P < 0.01$), confirming exceptionally high TCA cycle flux for 4HB assimilation (Fig. 4B). We further confirmed

metabolic remodeling through carbon mapping combined with ¹³C-metabolomics (Fig. 4C-E).

Regarding metabolic remodeling through anaplerosis inferred from changes of Pyc abundance, we determined the relative fraction of OAA derived from pyruvate by tracking triply ¹³C-labeled OAA (via aspartate labeling), which would be generated only from the carboxylation of triply

¹³C-labeled pyruvate by unlabeled CO₂ (Fig. 4C). At the plateau of the kinetic ¹³C data, we recorded 38% triply ¹³C-labeled pyruvate and 6% triply ¹³C-labeled aspartate in the SUC-fed cells (Fig. 4B), reflecting that 16% of OAA was derived from pyruvate (Fig. 4C), consistent with previous flux analysis⁶⁰. However, the isotopologue profiling in cells fed on the phenolic substrates revealed 30–45% of OAA derived from pyruvate (Fig. 4C), thus highlighting the increase in Pyc-catalyzed pyruvate carboxylation to OAA (i.e., anaplerosis) implied by the proteomics data.

To verify metabolic remodeling through the glyoxylate shunt, we illustrated carbon mapping for two scenarios. In one scenario, the metabolite SUC generated exclusively through the canonical TCA cycle with no flux through the glyoxylate shunt would result in non-labeled, singly ¹³C-labeled, triply ¹³C-labeled, and fully ¹³C-labeled SUC after one cycle of carbon mapping (Fig. 4D); an additional cycle would generate the same isotopologues (SI, Fig. S4). In another scenario, the glyoxylate shunt in the TCA cycle would generate doubly ¹³C-labeled SUC through isocitrate lyase (AceA) (Fig. 4E). Detection of this doubly ¹³C-labeled isotopologue only in the cells fed on the phenolic substrates confirmed the activation of the glyoxylate shunt during the metabolism of these substrates (Fig. 4B). Taken collectively, the findings from both the proteomics data and the ¹³C-metabolomics data delineated the operational metabolic network for phenolic acid utilization. To gain quantitative insights into the carbon and energy fluxes through the metabolic network, we performed ¹³C-fluxomics to obtain the fluxes through the different metabolic reactions and subsequently mapped out the cofactor balancing.

Remodeling of TCA cycle-associated fluxes sustains required cofactor balancing and ATP surplus

The algorithm for the ¹³C-fluxomics of each of the four phenolic acid substrates was constrained by biomass growth rates, substrate depletion rates, metabolite secretion rates, intracellular metabolite levels, and kinetic ¹³C-profiling of metabolites (Fig. 5A–D). Relative to SUC metabolism, the phenolic substrates generate influxes of acetyl-CoA from both the aromatic cleavage through the β-ketoadipate pathway and the acyl group in the hydroxycinnamates (FER and COU) (Fig. 1A). Consequently, the citrate synthase flux, which combines OAA with acetyl-CoA to form citrate, was up to 2-fold higher for the catabolism of the hydroxycinnamate compounds (FER and COU) than for the catabolism of the hydroxybenzoate compounds (VAN and 4HB) (Fig. 5A–D). Accordingly, citrate and α-ketoglutarate levels were up to 10-fold and 7-fold higher ($P < 0.001$), respectively, in cells grown on phenolic substrates than on SUC, implying high carbon flux towards the high energy-producing side of the TCA cycle (SI, Table S4). Notably, flux through the glyoxylate shunt was determined to be 2.5-fold to 13-fold higher during metabolism of the hydroxycinnamates than the hydroxybenzoates (Fig. 5A–D), consistent with our proteomics data on the relative abundance of AceA in the glyoxylate shunt during growth on the different types of phenolic acid substrates (Fig. 3C; SI, Table S3).

With respect to the flux remodeling at the cataplerosis-anaplerosis nodes, the cataplerotic flux through malic enzyme was 1.4-fold to 2.5-fold higher during phenolic substrate catabolism compared to SUC catabolism, while there was no flux through OAA decarboxylase (Fig. 5A–D; SI, Fig. S6). In fact, our intracellular metabolomics data revealed that intracellular malate decreased by up to 70% ($P < 0.05$), while PEP and 3-phosphoglycerate (3PG) increased 2-fold to 60-fold ($P < 0.01$) during phenolic substrate utilization, relative to SUC utilization, indicating strong cataplerotic flux from the TCA cycle towards intermediates in gluconeogenesis (SI, Table S4). Informed by the proteomics data, which highlighted up to 6-fold increase in Pyc (pyruvate carboxylase) relative to less than 2-fold increase in Ppc (PEP carboxylase) ($P < 0.001$) (Fig. 5), anaplerotic flux was constrained to occur only via Pyc, involving the carboxylation of pyruvate to OAA, to replenish four-carbon intermediates in the TCA cycle. This pyruvate-to-OAA anaplerotic flux was 7-fold to 20-fold higher during phenolic substrate utilization than SUC utilization (Fig. 5A–D; SI, Fig. S6), in agreement with the 2-fold to 3-fold higher OAA production from

pyruvate influx illustrated by the carbon mapping combined with kinetic ¹³C-metabolomics (Fig. 4C). For resolving whether to include flux through pyruvate dehydrogenase, we performed additional ¹³C-fluxomics with and without the reaction of pyruvate to acetyl-CoA (SI, Table S5). The model fit was not statistically acceptable when we deactivated this reaction in FER and COU (SI, Table S5), suggesting possible sufficient protein abundance to support flux or post-translational regulation^{41,61}. Therefore, pyruvate dehydrogenase was considered active during the phenolic substrate catabolism despite the observed decrease in the protein abundance (Fig. 3C).

We compared our high-resolution ¹³C-fluxomics of the metabolic network with the widely used approach of flux balance analysis (FBA), which is based only on substrate uptake and biomass growth rates and is thus derived from a low-resolution algorithm (Fig. 5A–D, Supplementary Data 4). In both ¹³C-fluxomics and FBA, sustenance of high TCA cycle flux was prioritized over gluconeogenic flux during phenolic substrate catabolism (Fig. 5A–D; Supplementary Data 4). Specifically, the ¹³C-fluxomics predicted that although the cataplerotic flux through malic enzyme (i.e., from malate to pyruvate) was substantial (60–80% of the carbon influx to malate), only 13–16% of this cataplerotic flux was invested towards gluconeogenic flux because 69–77% was recycled back to the TCA cycle via both pyruvate carboxylase (to replenish OAA) and pyruvate dehydrogenase (to generate acetyl-CoA) (Fig. 5A–D). The FBA still predicted 78–86% of carbon retention in the TCA cycle, but this was due to high malate dehydrogenase flux (from malate to OAA), while the cataplerotic malic enzyme flux was predicted to be low by the FBA. We attributed this difference between our ¹³C-fluxomics and the FBA modeling to the low resolution of the anaplerosis-cataplerosis node in the FBA algorithm (Supplementary Data 4).

With respect to relationships between our ¹³C-fluxomics and proteomics data, there was a general trend of positive correlation between changes in protein abundances and changes in fluxes in cataplerosis, anaplerosis, 4 reactions in gluconeogenesis, and at least 7 reactions in the TCA cycle (Fig. 5E). However, due to the discrepant magnitudes in the respective protein abundance changes and flux changes, there was an overall poor 1:1 correlation (Pearson correlation, $r = 0.11\text{--}0.35$, $P = 0.08\text{--}0.59$) (Fig. 5E). For instance, although carbon flux through isocitrate dehydrogenase increased 5-fold to 8-fold during growth on the phenolic acids compared to SUC, there was less than 2-fold change in the enzyme abundance. Serine phosphorylation was previously implicated in modulating flux through isocitrate dehydrogenase in *P. putida* KT2440 grown on a glucose:benzoate mixture versus glucose alone⁴¹. The discrepancy between changes in enzyme abundance and metabolic fluxes in our correlation matrices were thus consistent with the proposal that metabolic fluxes in central carbon metabolism are driven primarily by thermodynamic factors and post-translational modifications^{41,61}.

To examine consequences of the remodeled metabolic network on cofactor balance, we determined the rates of production and consumption of NADPH, NADH/UQH₂, and ATP during the catabolism of the phenolic substrates compared to SUC, as a reference (Fig. 6A). Due to reported absence of flux through oxPPP during gluconeogenic growth⁴⁸, as illustrated in Fig. 1A and confirmed by our ¹³C-fluxomics illustrated in Fig. 5A–D, cofactor production through oxPPP was not a contributing factor in our cofactor balancing for phenolic acid metabolism. Furthermore, water-forming NADH oxidase was not included in the cofactor balancing, based on a previous report of its minimal to no impact on metabolic flux distribution in *P. putida* KT2440⁴². Increased flux through cataplerosis via malic enzyme and through isocitrate dehydrogenase in the TCA cycle led to 1.2-fold to 2.5-fold greater NADPH production in cells grown on phenolic substrates compared to SUC-grown cells (Fig. 6A). As a result, the NADPH production was 24–44% in excess of the NADPH demand for both biomass synthesis and the peripheral pathway for aromatic substrate catabolism, including formaldehyde detoxification; this NADPH surplus was routed to NADH synthesis through transhydrogenase reactions (Fig. 6A). Due to the promoted retention of carbon flux in the TCA cycle, NADH/UQH₂ production was 1.4-fold to 2.7-fold higher during catabolism of phenolic substrates relative to SUC utilization (Fig. 6A). The NADH surplus was

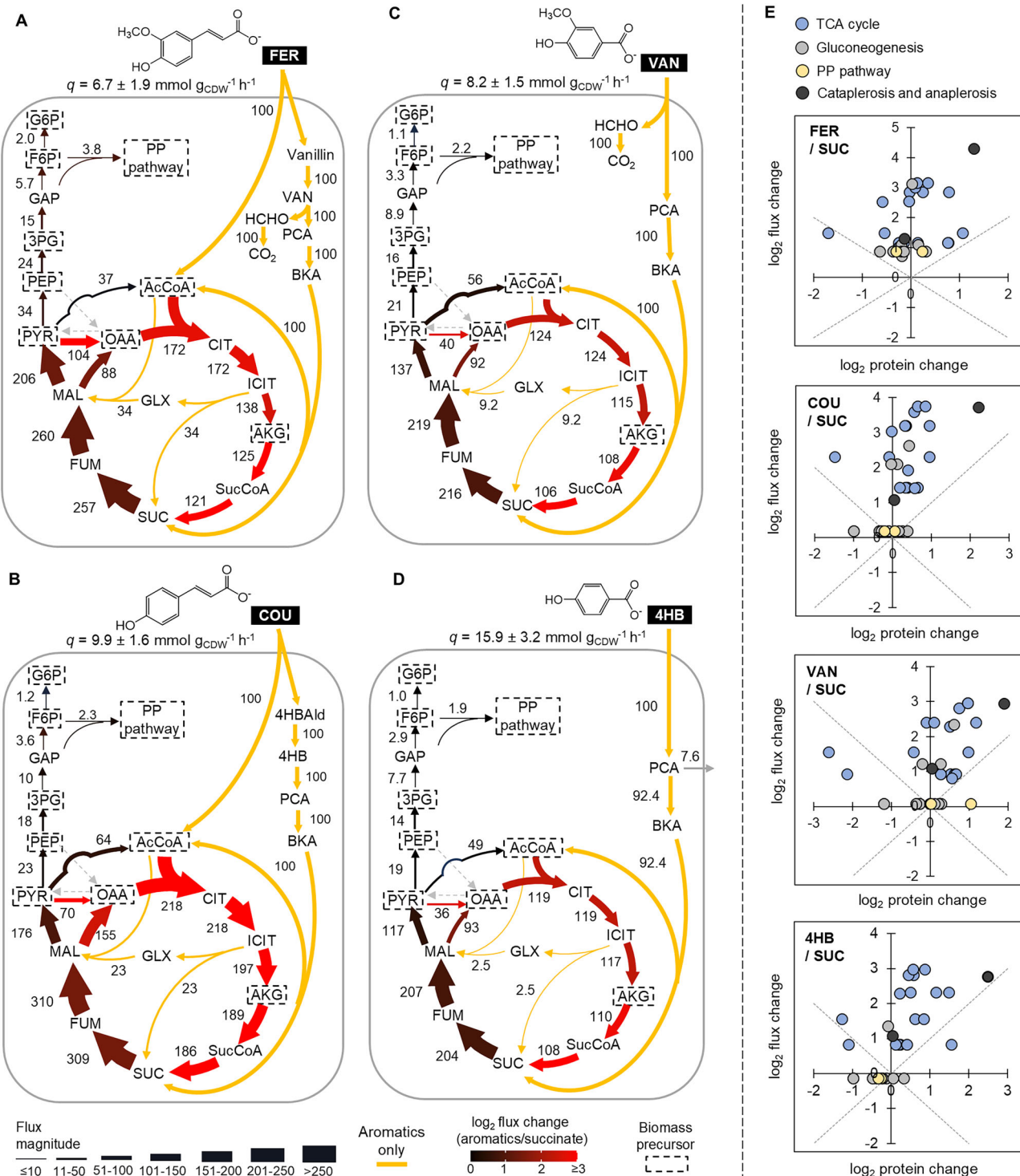


Fig. 5 | Quantitative flux analysis of the reaction network in phenolic acid metabolism revealed structure of the cataplerosis-anaplerosis nodes to sustain high flux in the TCA cycle. Metabolic flux analysis of *P. putida* KT2440 grown on A FER, B COU, C VAN, and D 4HB as the sole carbon source constrained by proteomics, metabolite pool sizes, and ¹³C metabolomics data. E Correlation matrices of relative flux changes versus relative protein abundance changes. All fluxes are normalized to the substrate uptake rate (q). The weight of arrows is relative to flux magnitude. Relative flux changes between cells grown on the phenolic

substrates and SUC are denoted by a blue-black-red color scheme. Increased flux is shown in shades of red, decreased flux is shown in shades of blue, and black indicates negligible differences in flux values. The yellow arrows represent fluxes that are predicted to be only in phenolic acid catabolism. The gray arrow represents metabolic secretion. Flux model of *P. putida* grown on SUC is provided in SI, Fig. S6. The complete flux estimations are provided in Supplementary Data 3. Abbreviations of metabolites are the same as shown in the main text.

1.4-fold to 2.7-fold higher in phenolic substrate-fed cells than SUC-grown cells, resulting in a corresponding fold increase in ATP production via oxidative phosphorylation (Fig. 6A). In corroboration of the model-predicted ATP surplus, absolute quantitation of the intracellular ATP

content revealed up to 2-fold higher ATP in cells fed with FER, COU, or 4HB than in the SUC-fed cells ($P < 0.01$); the lack of similar trend with VAN implied unaccounted ATP demand, likely related to additional ATP needed to cope with oxidative stress during VAN assimilation⁶² (Fig. 6A, B). The

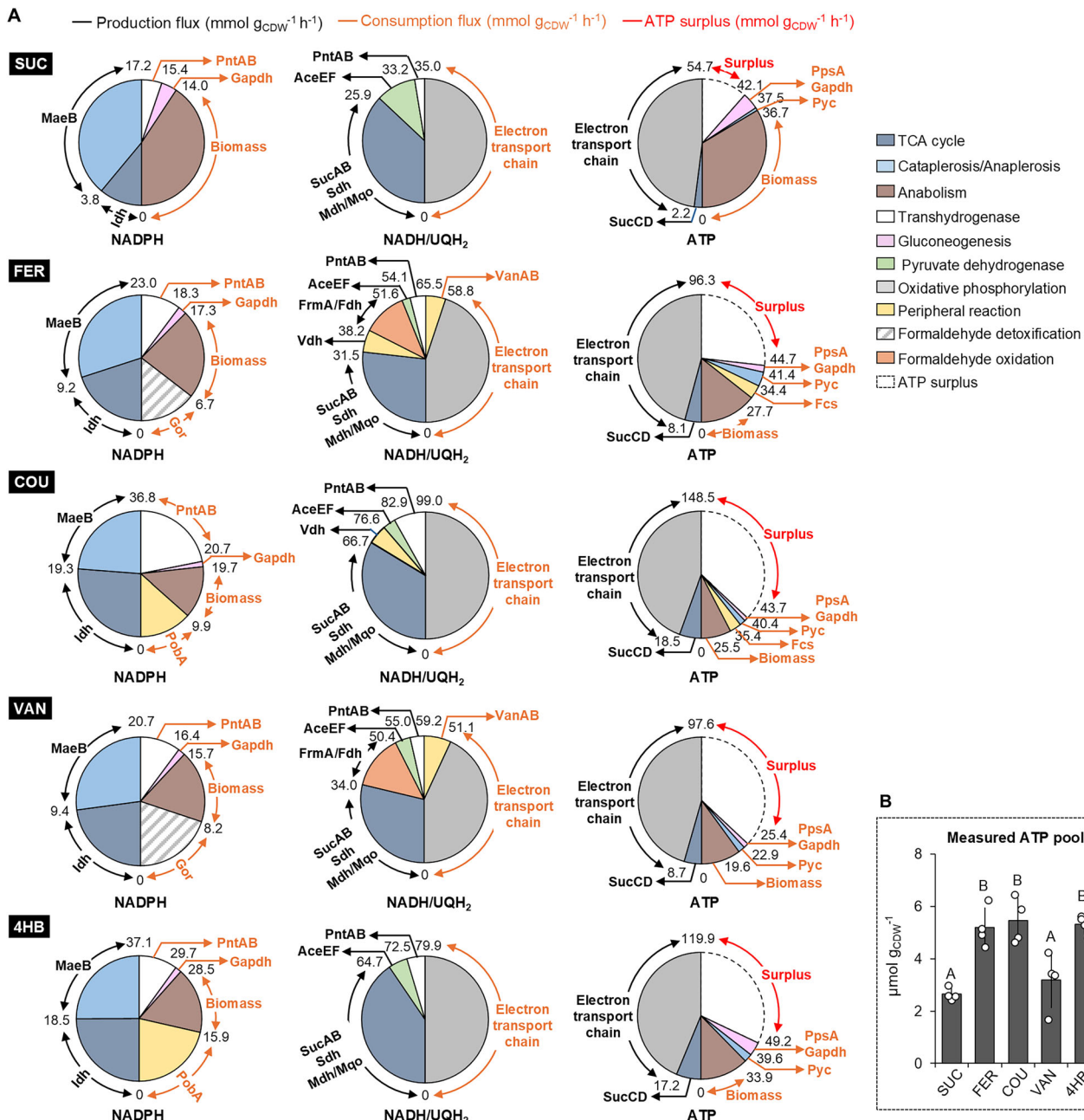


Fig. 6 | Quantitative mapping of metabolic reactions in cofactor flux balancing during processing of four lignin-derived phenolic acid substrates compared to succinate. **A** Production (black) and consumption (orange) fluxes ($\text{mmol g}_{\text{CDW}}^{-1} \text{ h}^{-1}$) of NADPH, NADH/UQH₂, and ATP during growth on, from top to bottom, SUC, FER, COU, VAN, and 4HB. **B** Quantified intracellular ATP pool size ($\mu\text{mol g}_{\text{CDW}}^{-1}$) in cells grown on the lignin-related phenolic substrates compared to succinate. In **A**, the numbers of the pie chart indicate the flux values ($\text{mmol g}_{\text{CDW}}^{-1} \text{ h}^{-1}$); the metabolic proteins and pathways involved in each reaction are

specified near the pie charts and in the color legends, respectively. In **A**, production of ATP from NADH/UQH₂ was calculated using a phosphate to oxygen (P/O) ratio of 1.5. Details of flux data in **(A)** were provided in SI, Table S6. Data in **(B)** are expressed as mean \pm standard deviation from four independent biological replicates ($n = 4$) and one-way ANOVA was performed followed by Tukey's HSD post hoc test; statistically significant differences ($P < 0.05$) are denoted by a change in letter. Detailed data in **(B)** were provided in SI, Table S1.

surplus of ATP predicted by the flux model, which was confirmed by independent measurements of intracellular ATP, was consistent with the relatively higher energy charge values during processing of the phenolic substrates compared to SUC (SI, Fig. S2), underscoring the optimization of the carbon metabolism in *P. putida* to maintain a high-energy state during phenolic substrate utilization.

Discussion

The catabolism of lignin-derived phenolic substrates represents a critical step in valorizing lignin using biotechnologically relevant microbes^{2–4}.

Strains of *P. putida* are extensively studied for this endeavor due to their native ability to catabolize various aromatic compounds⁵. However, elucidation of the native metabolic network in relation to cofactor balance in *P. putida* during catabolism of phenolic substrates remains a knowledge gap. Here, we performed a comprehensive quantitative analysis of the metabolic underpinnings of carbon and energy fluxes in *P. putida* KT2440 during conversion of two hydroxycinnamates and two hydroxybenzoates, which represent common lignin-derived phenolic substrates.

To address metabolic bottlenecks during conversion of phenolic substrates, increase in enzyme expression was shown to be a successful strategy

when an enzyme (i.e., VanA or VanB) exhibited a preference for NADH over NADPH, but bottleneck was not alleviated for an enzyme (i.e., PobA) with NADPH specificity due to cofactor deficiency^{17,21,29,32}. The latter deficiency was circumvented by substituting for an enzyme with broader cofactor specificity (i.e., Pral) or by increasing NADPH supply through substrate co-feeding^{30,32}. Our quantitative flux analysis determined that the metabolic fluxes generated excess in both NADPH and NADH in *P. putida* KT2440, but the NADH surplus was up to 6-fold higher than the NADPH surplus. Thus, our findings implied that the native cofactor balance was more amenable to buffering increased NADH demand than increased NADPH demand from enzyme overexpression. These findings inform rational design of metabolic engineering strategies, particularly when targeting fluxes through isoenzymes with similar catalytic functions but with distinct cofactor preferences. The surplus of NAD(P)H can benefit bio-production of free fatty acids⁶³ and polyhydroxyalkanoates⁶⁴, while ATP overproduction can be employed in improving yield of biopolymers that require energy input, such as ϵ -Poly-L-lysine⁶⁵. Predicted by our proteomics data and confirmed by ¹³C-fluxomics, we identified key nodes of flux remodeling with important energetic consequences during the metabolism of the phenolic substrates. At the cataplerosis-anaplerosis nexus between the TCA cycle and gluconeogenesis, we found that *P. putida* KT2440 exhibited the specific cataplerotic routing of carbon fluxes through malic enzyme (to deplete malate and produce pyruvate) and anaplerotic routing through pyruvate carboxylase (to replenish OAA). Notably, the enhanced carbon flux through malic enzyme was critical in sustaining the necessary NADPH yield, but resulted in decreasing flux to OAA through malate dehydrogenase. As a consequence, one important role of the anaplerotic carbon recycling to the TCA cycle via pyruvate carboxylase was to satisfy OAA demand for biosynthesis. This adaptation of cataplerosis and anaplerosis generated 50% of the NADPH yield and sustained high flux through the TCA cycle to produce over 70% of the NADH yield, which eventually fueled oxidative phosphorylation for ATP production. A similar routing of carbon fluxes through the cataplerosis-anaplerosis nodes was noted in glucose-grown *P. putida* to satisfy elevated cofactor demands in response to oxidative and energetic stresses^{41,47}. For instance, in response to oxidative stress, *P. putida* has been shown to enhance carbon flux from glucose catabolism through the oxPPP to generate excess NADPH that exceeded 50% of the biomass demand⁴⁷. Moreover, when the conversion of NADH to ATP via oxidative phosphorylation was uncoupled chemically in glucose-fed *P. putida*, there was an increase in carbon flux through the high-energy producing side of the TCA cycle towards providing NAD(P)H and ATP production to counterbalance the metabolic perturbation⁴². Thus, we propose that cofactor-driven metabolic reprogramming is a widespread phenomenon under different substrate utilization.

The *ortho*-cleavage pathway, the only known catabolic route for the phenolic substrates in *P. putida* (particularly strain KT2440), generates SUC and acetyl-CoA to feed into the TCA cycle. There are two other reported aerobic PCA cleavage pathways: for example, the 2,3-*meta* cleavage pathway found in *P. putida* strains mt-2 and H, and the 4,5-*meta* cleavage pathway revealed in *Comamonas testosteroni* and *Sphingobium sp.* SYK-6^{61,66-69}. The 2,3-*meta* cleavage route generates pyruvate and acetyl-CoA with the production of NADH^{66,69}; the 4,5-*meta* cleavage route generates OAA and pyruvate with the production of NADPH^{61,68}. The quantitative analysis employed here to decode cofactor balance involved in the *ortho*-cleavage pathway could be used to evaluate the metabolic routing of phenolic carbons and cellular cofactor balance following the other cleavage pathways.

In sum, we unraveled quantitatively the interplay between carbon metabolism and energy metabolism in *P. putida* KT2440 grown on lignin-derived phenolic acid substrates, focusing on the catabolism of hydroxycinnamates and hydroxybenzoates with PCA as the common catabolic intermediate. Lignin-derived compounds can also constitute of other aromatic structures⁵, with different intermediates such as catechol and gallate⁶. Moreover, sugar monomers and aliphatic acids often co-exist with phenolic acids in hydrolysates of lignocellulosic feedstocks^{70,71}. Therefore, a valuable next step is the investigation of the energy metabolism in *P. putida* during

co-utilization of different phenolic structures with sugars or aliphatic acids. To this end, the current research findings provide a valuable quantitative blueprint of the native metabolic network and its tuning of carbon and energy fluxes for further interrogations and explorations of Pseudomonads and other related bacterial platforms for lignocellulose valorization.

Methods

Bacterial cultivation

P. putida (strain KT2440) was obtained from the American Type Culture Collection (ATCC) and stored in Lysogeny broth (Miller) nutrient-rich medium with 25% glycerol at -80 °C. Cells were washed and inoculated from frozen stocks into 20-mL glass tubes that contained 5 mL of pH-adjusted (7.0) minimal nutrient medium with the same carbon-equivalent concentration, 100 mM C, of each substrate as a sole source of carbon: FER, COU, VAN, 4HB or SUC. The minimal nutrient medium contained 5.0 mM Na₂HPO₄, 20 mM K₂HPO₄, 37 mM NH₄Cl, 17 mM NaCl, 0.81 mM MgSO₄·7H₂O, and 34 μM CaCl₂·2H₂O. Addition of essential trace metal nutrients and FeSO₄ (30 μM) to the nutrient medium was done prior to inoculation. After initial inoculation of the culture in glass tubes at 30 °C with shaking at 220 rpm overnight in an incubator-shaker (New Brunswick Scientific, Edison, NJ)⁴⁸, the cells were harvested, washed and subsequently transferred into 125-mL or 250-mL baffled flasks. To optimize oxygen transfer, only one-fifth of the volume of the baffled flask was filled with the minimal nutrient medium with carbon source. Cell growth was monitored by measuring the optical density at 600 nm (OD₆₀₀) using an Agilent Cary UV-Vis spectrophotometer (Santa Clara, CA). Cell dry weight per gram (g_{CDW}) was measured by weighing the mass of lyophilized cell pellets collected throughout the growth⁴⁸. The conversion factor of OD₆₀₀ and g_{CDW} was calculated through linear regression with R² coefficient greater than 0.80⁴⁸. All growth experiments were conducted in three biological replicates.

Mutant construction

Construction details for strains, oligonucleotides, and plasmids are detailed in SI, Tables S7–S9. In brief, all plasmids were synthesized and cloned by Twist Biosciences. Ribosome binding sites were optimized for each native *P. putida* KT2440 sequence⁷². For the construction of *P. putida* strains, the parental strain *P. putida* AG5577 containing a total of nine unique attB sites was used⁷³. The parental strain *P. putida* AG5577 was confirmed to be identical to the wild-type *P. putida* KT2440 in phenolic acid utilization (SI, Fig. S2). All integrations were achieved by serine recombinase-assisted genome engineering using either the BxB1 or TG1 recombinase^{73,74}. Integrations were confirmed using Oxford Nanopore sequencing at Plasmidsaurus (<https://www.plasmidsaurus.com>).

Measuring extracellular substrate depletion

Aliquots of cell suspensions were collected and spanned at different time points throughout biomass growth. Following filtering during centrifugation (Costar Spin-X, 0.22-μm-pore-size filter), the filtrates were stored at -20 °C until analysis. The concentration of each aromatic substrate was determined using ultra-high-performance liquid chromatography (UHPLC) with an Agilent ZORBAX Eclipse Plus C18 column (4.6 × 100 mm with 5 μm particle size) and a UV detector at 210 nm for 4HB and VAN detection, and 275 nm for FER and COU detection. The injection volume was 10 μL and the column was maintained at 25 °C. The mobile phase consisted of 0.1% formic acid (eluent A) and 80:10:10 acetonitrile: methanol: H₂O (v/v) (eluent B) with a flow rate of 0.9 mL·min⁻¹. The gradient of eluent B was set as 0 min, 6%; 6.5 min, 15%; 8.5 min, 25%; 10.75 min, 37.5%; 15.5 min, 65%; 16.25 min, 6%. Extracellular substrate depletion rate, in mmol g_{CDW}⁻¹ h⁻¹, was determined by regression analysis. The rate of SUC depletion was obtained by Wilkes et al.⁴⁸.

Quantitative proteomics

P. putida KT2440 was cultured until mid-exponential phase (OD₆₀₀ = 1.0–1.2) using 100 mM C of FER, COU, VAN, 4HB, or SUC as the sole carbon source in the nutrient minimal medium. After centrifugation of

2-mL cultures ($10,000 \times g$ for 5 min at 4°C), the cell pellets were washed twice with phosphate-buffered solution (pH = 7.4) within 10 min to remove extracellular components followed by quenching with cold methanol (4°C) and incubated on ice for 30 min⁷⁵. Samples were kept on ice to minimize protein change during the processing. The quenched cell suspensions were centrifuged, and the pellets were resuspended in methanol and stored at -80°C until analysis.

The samples were processed with an on-filter in-cell (OFIC) digestion approach⁷⁶. Briefly, after transferring the samples to E3 filters (CDS Analytical, Oxford, PA), and centrifuging ($400 \times g$ for 1 min), the filter was washed once with methanol, and treated with 10 mM Tris(2-carboxyethyl)phosphine and 40 mM chloroacetamide (in 50 mM triethylammonium bicarbonate, TEAB), followed by incubating at 45°C for 10 min. The sample-containing filters were spun to remove liquid, followed by washing once with 50 mM TEAB. Subsequently, the samples were digested with Trypsin/LysC mix at 37°C for 16–18 h. After digestion, the peptides were eluted, pooled, and dried in SpeedVac. The peptides were desalted with StageTips (CDS Analytical, Oxford, PA), dried, and stored at -80°C until further analysis.

The peptides were first loaded onto a trap column (PepMap100 C18, 300 $\mu\text{m} \times 2 \text{ mm}$ with 5 μm particle size; Thermo Scientific) then separated through an analytical column (PepMap100 C18, 50 cm \times 75 μm with 3 μm particle size; Thermo Scientific) with eluents consisting of 0.1% formic acid in water (v/v) (eluent A) and 0.1% formic acid in acetonitrile (v/v) (eluent B) with a flow rate of 250 nL·min⁻¹ using an Ultimate 3000 RSLC nano system with nano electrospray ionization for liquid chromatography mass spectrometry analysis (LC-MS). The MS data were acquired on an Orbitrap Eclipse mass spectrometer with FAIMS Pro Interface (Thermo Scientific) at 120 K resolution, followed by MS/MS acquisition in data-independent mode following a FAIMS-DIA proteomic pipeline⁷⁷.

The mass spectrometry data were processed using Spectronaut software (version 19.1)⁷⁸ and a library-free DIA analysis workflow with directDIA+ and the *P. putida* KT2440 protein sequence (Uniprot 2024 release; 5950 sequences). In short, the settings for Pulsar and library generation included: Trypsin/P as specific enzyme; peptide length from 7 to 52 amino acids; allowing 2 missed cleavages; toggle N-terminal M turned on; Carbamidomethyl on C as fixed modification; Oxidation on M and Acetyl at protein N-terminus as variable modifications; FDRs at PSM, peptide and protein level all set to 0.01; Quantity MS level set to MS2, and cross-run normalization turned on. Bioinformatics analyses were performed using Perseus software (version 1.6.2.3)⁷⁹. The full dataset of proteomics is provided in Supplementary Data 1.

Intracellular metabolite levels and isotope labeling kinetics

To profile the intracellular metabolites of each of the substrate condition (100 mM C of FER, COU, VAN, 4HB, or SUC), cell suspensions (3 mL) of *P. putida* KT2440 during mid-exponential growth phase ($\text{OD}_{600} = 1.0\text{--}1.2$) were filtered (0.22 μm nylon membranes; Whatman, 7402-004), then lysed in a cold solvent (4°C) containing methanol, acetonitrile, and water in a 2:2:1 (v/v) ratio. Metabolism was quenched by submerging the filter containing the cells immediately in the cold solvent mixture, which lysed the cells; there was less than 1 min between the filtering process and the transfer of the filter to the cold solvent. This well-established protocol⁸⁰ for metabolite extraction after quenching metabolism was illustrated previously by the senior author^{41,48,60,61,81,82} and others^{83–85}. The suspensions with the lysed cells were centrifuged ($10,000 \times g$, 4°C for 5 min) and aliquots (200 μL) of the supernatants in 2 mL-tubes were dried under ultrapure nitrogen gas followed by storage at -80°C before further analysis. The dried samples, collected from four biological replicates, were resuspended in 100 μL LC-MS grade water before metabolomics analysis.

In preparation for kinetic ^{13}C -labeling experiments, 3-mL exponentially-growing *P. putida* KT2440 cells (two transfers, three biological replicates) on each unlabeled substrate (100 mM C of FER, COU, VAN, 4HB, or SUC) were filtered (0.22 μm nylon membranes; Whatman, 7402-004), and the filters containing the cells were placed onto agar plates containing 100 mM C of the same substrate, followed by incubation at 30°C until

exponential growth was resumed. To initiate ^{13}C -labeling of intracellular metabolites, cell-containing filters were transferred onto fresh agar plates with 50% of ^{13}C -labeled substrate: $^{13}\text{C}_6$ -phenyl-FER, $^{13}\text{C}_6$ -phenyl-COU, $^{13}\text{C}_6$ -phenyl-VAN, $^{13}\text{C}_6$ -phenyl-4HB, or U $^{13}\text{C}_4$ -succinate. These labeled substrates were purchased from Cambridge Isotopes (Tewksbury, MA) or Sigma-Aldrich (St. Louis, MO). At four different time points (15 s, 1 min, 5 min, and 15 min), cells adhered to the filter were quenched into the aforementioned cold quenching solution (4°C); data for time 0 were obtained with cells directly quenched from the unlabeled plate. The quenched cell suspensions were processed following the aforementioned nitrogen drying procedure and the extracted metabolites were stored at -80°C until metabolomics analysis.

Metabolomics analysis

Intracellular and extracellular metabolites were quantified based on our established metabolomics protocol using UHPLC (Thermo Fisher Scientific Dionex UltiMate 3000) coupled with high-resolution mass spectrometry (Thermo Fisher Scientific Q Exactive quadrupole-Orbitrap) operating in negative mode^{48,81}. The LC column, an Acquity UPLC BEH C18 Column (particle size 1.7 μm , 2.1 mm \times 100 mm, Waters), was maintained at 25°C with an injection volume of 10 μL . The eluents contained 97:3 (v/v) LC-MS grade water:methanol with 15 mM acetic acid and 10 mM tributylamine (solvent A) and methanol (solvent B)⁸¹. The flow rate was set at 0.18 mL·min⁻¹⁸¹. The data was analyzed on the Thermo Scientific XCalibur software (v3.0) using a series of standard concentrations. The fraction of different isotopomers was analyzed using the Metabolomic Analysis and Visualization Engine software version 2011.6.17⁸⁶; to correct for the natural abundance of ^{13}C , IsoCor v2.2.0⁸⁷ was used. The full dataset of kinetic ^{13}C -metabolomics is provided in Supplementary Data 2.

^{13}C -fluxomics analysis

We employed both the levels and the kinetic isotopic profiling of intracellular metabolites to perform an isotope non-steady state metabolic flux analysis (INST-MFA)³⁷. A core *P. putida* metabolic network was constructed based on published resources with modifications to supplement aromatics utilization pathways^{46,49}. The biomass yield equation was modified from a previous genome scale model for *P. putida* KT2440⁸⁸. The INCA software (v2.3) based on the Matlab platform⁸⁹ was used to simulate isotopomer balances when *P. putida* was fed on different aromatic substrates and succinate. The INST-MFA models were constrained with growth, substrate consumption and metabolite secretion rates, measured pool sizes (CIT, AKG, SUC, PYR, PEP, 3PG, G6P, AcCoA) and kinetic isotopomer distributions (CIT, AKG, SUC, OAA as aspartate, PEP, PYR, 3PG, DHAP, G6P, S7P, AcCoA). Flux estimations were reiterated at least 50 times from random initial values. At least three independent flux estimations were performed for each INST-MFA model to ensure the flux estimations were consistent. The estimates were considered as statistically acceptable fits when the results passed the χ^2 goodness-of-fit test (cutoff 95% confidence level), i.e., the minimized variance-weighted sum of squared residuals (SSR) were within the expected range. The standard errors (95% confidence intervals) of the flux estimations for the reactions in the central carbon metabolism were calculated through the Monte Carlo simulation module associated with the INCA software^{49,89}. Complete flux estimations are in Supplementary Data 3. Cofactor balance was calculated from quantified fluxes for metabolic reactions with production or consumption of NADPH, NADH/UQH₂, and ATP. Only NADH was included for vanillate *O*-demethylase because VanB was shown to prefer NADH over NADPH¹⁷.

Flux balance analysis

The most recent genome-scale model of *P. putida* KT2440 (iJN1463) was downloaded from the BIGG database (<http://bigg.ucsd.edu/>)⁸⁸. The FER, VAN, and 4HB catabolic reactions are present in the original iJN1463 model. The COU uptake and initial catabolic reactions to coumaroyl-CoA were added manually to the model. The optimized flux distribution predicted by FBA was performed using the COBRAPy library (version 0.29.1)⁹⁰.

Substrate uptake rates for SUC, FER, COU, VAN, and 4HB were fixed at the experimentally determined values (in mmol/g_{CDW}/h), which are 16.0, 6.7, 9.9, 8.2, and 15.9, respectively. For the 4HB analysis, the PCA secretion rate was fixed at 1.2 mmol/g_{CDW}/h as experimentally measured. Results for FBA are in Supplementary Data 4.

Statistics and reproducibility

All experimentally measured data were expressed as mean \pm standard deviation of three or four biological replicates (as indicated in figure captions). Unpaired two-tailed *t*-test was applied to evaluate the significance of differences between two groups. One-way analysis of variance (ANOVA) was used to evaluate differences among three or more conditions. Tukey's honestly significant difference post hoc test was performed for pairwise comparison in addition to one-way ANOVA. The *P* value threshold for statistically significant difference was set at 0.05.

Reporting summary

Further information on research design is available in the Nature Portfolio Reporting Summary linked to this article.

Data availability

Proteomics MS data are freely available via ProteomeXchange server (<https://www.proteomexchange.org/>) under accession PXD067246 and the MassIVE repository (<https://massive.ucsd.edu/>) under accession MSV000098800. Metabolomics MS data are available through the MetaboLights depositary (<https://www.ebi.ac.uk/metabolights/>) under accession number MTBLS11484. All source data for the figures were provided in Supplementary Data 5, and all other data are available from the corresponding author on reasonable request.

Code availability

Custom code for FBA analysis can be accessed through GitHub repository (https://github.com/nqzhou/Aromatics_fba) and Zenodo repository (<https://doi.org/10.5281/zenodo.16793025>).

Received: 23 April 2025; Accepted: 13 August 2025;

Published online: 29 August 2025

References

- Ragauskas, A. J. et al. Lignin valorization: improving lignin processing in the biorefinery. *Science* **344**, 1246843 (2014).
- Beckham, G. T., Johnson, C. W., Karp, E. M., Salvachúa, D. & Vardon, D. R. Opportunities and challenges in biological lignin valorization. *Curr. Opin. Biotechnol.* **42**, 40–53 (2016).
- Kamimura, N. et al. Bacterial catabolism of lignin-derived aromatics: new findings in a recent decade: update on bacterial lignin catabolism. *Environ. Microbiol. Rep.* **9**, 679–705 (2017).
- Becker, J. & Wittmann, C. A field of dreams: lignin valorization into chemicals, materials, fuels, and health-care products. *Biotechnol. Adv.* **37**, 107360 (2019).
- Schutyser, W. et al. Chemicals from lignin: an interplay of lignocellulose fractionation, depolymerisation, and upgrading. *Chem. Soc. Rev.* **47**, 852–908 (2018).
- Jiménez, J. I., Miñambres, B., García, J. L. & Díaz, E. Genomic analysis of the aromatic catabolic pathways from *Pseudomonas putida* KT2440. *Environ. Microbiol.* **4**, 824–841 (2002).
- Nikel, P. I. & de Lorenzo, V. *Pseudomonas putida* as a functional chassis for industrial biocatalysis: from native biochemistry to *trans*-metabolism. *Metab. Eng.* **50**, 142–155 (2018).
- Schwanemann, T., Otto, M., Wierckx, N. & Wynands, B. *Pseudomonas* as versatile aromatics cell factory. *Biotechnol. J.* **15**, 1900569 (2020).
- de Lorenzo, V., Pérez-Pantoja, D. & Nikel, P. I. *Pseudomonas putida* KT2440: the long journey of a soil-dweller to become a synthetic biology chassis. *J. Bacteriol.* **0**, e00136–24 (2024).
- Silva, M., Donati, S. & Dvořák, P. Advances in engineering substrate scope of *Pseudomonas* cell factories. *Curr. Opin. Biotechnol.* **92**, 103270 (2025).
- Kim, G. B., Kim, H. R. & Lee, S. Y. Comprehensive evaluation of the capacities of microbial cell factories. *Nat. Commun.* **16**, 2869 (2025).
- Ravi, K., García-Hidalgo, J., Gorwa-Grauslund, M. F. & Lidén, G. Conversion of lignin model compounds by *Pseudomonas putida* KT2440 and isolates from compost. *Appl. Microbiol. Biotechnol.* **101**, 5059–5070 (2017).
- Wada, A. et al. Characterization of aromatic acid/proton symporters in *Pseudomonas putida* KT2440 toward efficient microbial conversion of lignin-related aromatics. *Metab. Eng.* **64**, 167–179 (2021).
- Salvachúa, D. et al. Outer membrane vesicles catabolize lignin-derived aromatic compounds in *Pseudomonas putida* KT2440. *Proc. Natl. Acad. Sci. USA* **117**, 9302–9310 (2020).
- Erickson, E. et al. Critical enzyme reactions in aromatic catabolism for microbial lignin conversion. *Nat. Catal.* **5**, 86–98 (2022).
- Nichols, N. N. & Harwood, C. S. PcaK, a high-affinity permease for the aromatic compounds 4-hydroxybenzoate and protocatechuate from *Pseudomonas putida*. *J. Bacteriol.* **179**, 5056–5061 (1997).
- Bleem, A. C. et al. Evolution and engineering of pathways for aromatic O-demethylation in *Pseudomonas putida* KT2440. *Metab. Eng.* **84**, 145–157 (2024).
- Linger, J. G. et al. Lignin valorization through integrated biological funneling and chemical catalysis. *Proc. Natl. Acad. Sci. USA* **111**, 12013–12018 (2014).
- Graf, N. & Altenbuchner, J. Genetic engineering of *Pseudomonas putida* KT2440 for rapid and high-yield production of vanillin from ferulic acid. *Appl. Microbiol. Biotechnol.* **98**, 137–149 (2014).
- Vardon, D. R. et al. Adipic acid production from lignin. *Energy Environ. Sci.* **8**, 617–628 (2015).
- Salvachúa, D. et al. Bioprocess development for muconic acid production from aromatic compounds and lignin. *Green. Chem.* **20**, 5007–5019 (2018).
- Kohlstedt, M. et al. From lignin to nylon: cascaded chemical and biochemical conversion using metabolically engineered *Pseudomonas putida*. *Metab. Eng.* **47**, 279–293 (2018).
- Johnson, C. W. et al. Innovative chemicals and materials from bacterial aromatic catabolic pathways. *Joule* **3**, 1523–1537 (2019).
- Salvachúa, D. et al. Metabolic engineering of *Pseudomonas putida* for increased polyhydroxyalkanoate production from lignin. *Micro Biotechnol.* **13**, 290–298 (2020).
- Zhou, Y. et al. Development of a CRISPR/Cas9n-based tool for metabolic engineering of *Pseudomonas putida* for ferulic acid-to-polyhydroxyalkanoate bioconversion. *Commun. Biol.* **3**, 1–13 (2020).
- Almqvist, H. et al. Muconic acid production using engineered *Pseudomonas putida* KT2440 and a guaiacol-rich fraction derived from kraft lignin. *ACS Sustain. Chem. Eng.* **9**, 8097–8106 (2021).
- Eng, T. et al. Engineering *Pseudomonas putida* for efficient aromatic conversion to bioproduct using high throughput screening in a bioreactor. *Metab. Eng.* **66**, 229–238 (2021).
- Valencia, L. E. et al. Engineering *Pseudomonas putida* KT2440 for chain length tailored free fatty acid and oleochemical production. *Commun. Biol.* **5**, 1–12 (2022).
- Werner, A. Z. et al. Lignin conversion to β -ketoadipic acid by *Pseudomonas putida* via metabolic engineering and bioprocess development. *Sci. Adv.* **9**, eadj0053 (2023).
- Liu, H. et al. Engineering *Pseudomonas putida* for lignin bioconversion into *cis-cis* muconic acid. *Chem. Eng. J.* **495**, 153375 (2024).
- Banerjee, D. et al. Addressing genome scale design tradeoffs in *Pseudomonas putida* for biotransformation of an aromatic carbon source. *npj Syst. Biol. Appl.* **11**, 1–13 (2025).
- Kuatsjah, E. et al. Debottlenecking 4-hydroxybenzoate hydroxylation in *Pseudomonas putida* KT2440 improves muconate productivity from p-coumarate. *Metab. Eng.* **70**, 31–42 (2022).

33. Gómez-Álvarez, H. et al. Bioconversion of lignin-derived aromatics into the building block pyridine 2,4-dicarboxylic acid by engineering recombinant *Pseudomonas putida* strains. *Bioresour. Technol.* **346**, 126638 (2022).
34. Johnson, C. W. et al. Eliminating a global regulator of carbon catabolite repression enhances the conversion of aromatic lignin monomers to muconate in *Pseudomonas putida* KT2440. *Metab. Eng. Commun.* **5**, 19–25 (2017).
35. Wiechert, W. ¹³C Metabolic flux analysis. *Metab. Eng.* **3**, 195–206 (2001).
36. Wiechert, W. & Nöh, K. Isotopically non-stationary metabolic flux analysis: complex yet highly informative. *Curr. Opin. Biotechnol.* **24**, 979–986 (2013).
37. Jazmin, L. J. & Young, J. D. Isotopically nonstationary ¹³C metabolic flux analysis. *Methods Mol. Biol.* **985**, 367–390 (2013).
38. Hollinshead, W. D., Henson, W. R., Abernathy, M., Moon, T. S. & Tang, Y. J. Rapid metabolic analysis of *Rhodococcus opacus* PD630 via parallel ¹³C-metabolite fingerprinting. *Biotechnol. Bioeng.* **113**, 91–100 (2016).
39. Sacco, S. A. & Young, J. D. ¹³C metabolic flux analysis in cell line and bioprocess development. *Curr. Opin. Chem. Eng.* **34**, 100718 (2021).
40. Antoniewicz, M. R. A guide to metabolic flux analysis in metabolic engineering: methods, tools and applications. *Metab. Eng.* **63**, 2–12 (2021).
41. Kukuruya, M. A. et al. Multi-omics analysis unravels a segregated metabolic flux network that tunes co-utilization of sugar and aromatic carbons in *Pseudomonas putida*. *J. Biol. Chem.* **294**, 8464–8479 (2019).
42. Ebert, B. E., Kurth, F., Grund, M., Blank, L. M. & Schmid, A. Response of *Pseudomonas putida* KT2440 to Increased NADH and ATP Demand. *Appl. Environ. Microbiol.* **77**, 6597–6605 (2011).
43. Chavarría, M., Kleijn, R. J., Sauer, U., Pfleiderer-Grau, K. & de Lorenzo, V. Regulatory tasks of the phosphoenolpyruvate-phosphotransferase system of *Pseudomonas putida* in central carbon metabolism. *mBio* **3**, <https://doi.org/10.1128/mbio.00028-12> (2012).
44. Nikel, P. I., Chavarría, M., Fuhrer, T., Sauer, U. & de Lorenzo, V. *Pseudomonas putida* KT2440 strain metabolizes glucose through a cycle formed by enzymes of the Entner-Doudoroff, Embden-Meyerhof-Parnas, and Pentose Phosphate pathways. *J. Biol. Chem.* **290**, 25920–25932 (2015).
45. Sasnow, S. S., Wei, H. & Aristilde, L. Bypasses in intracellular glucose metabolism in iron-limited *Pseudomonas putida*. *MicrobiologyOpen* **5**, 3–20 (2016).
46. Kohlstedt, M. & Wittmann, C. GC-MS-based ¹³C metabolic flux analysis resolves the parallel and cyclic glucose metabolism of *Pseudomonas putida* KT2440 and *Pseudomonas aeruginosa* PAO1. *Metab. Eng.* **54**, 35–53 (2019).
47. Nikel, P. I. et al. Reconfiguration of metabolic fluxes in *Pseudomonas putida* as a response to sub-lethal oxidative stress. *ISME J.* **15**, 1751–1766 (2021).
48. Wilkes, R. A., Waldbauer, J. & Aristilde, L. Analogous metabolic decoupling in *Pseudomonas putida* and *Comamonas testosteroni* implies energetic bypass to facilitate gluconeogenic growth. *mBio* **12**, e03259–21 (2021).
49. Czajka, J. J. et al. Tuning a high performing multiplexed-CRISPRi *Pseudomonas putida* strain to further enhance indigoidine production. *Metab. Eng. Commun.* **15**, e00206 (2022).
50. Vogeeler, P. et al. Metabolic impact of heterologous protein production in *Pseudomonas putida*: insights into carbon and energy flux control. *Metab. Eng.* **81**, 26–37 (2024).
51. Dvořák, P. et al. Synthetically-primed adaptation of *Pseudomonas putida* to a non-native substrate D-xylose. *Nat. Commun.* **15**, 2666 (2024).
52. Sudarsan, S. et al. Dynamics of benzoate metabolism in *Pseudomonas putida* KT2440. *Metab. Eng. Commun.* **3**, 97–110 (2016).
53. Bonora, M. et al. ATP synthesis and storage. *Purinergic Signal* **8**, 343–357 (2012).
54. Owen, O. E., Kalhan, S. C. & Hanson, R. W. The key role of anaplerosis and cataplerosis for citric acid cycle function. *J. Biol. Chem.* **277**, 30409–30412 (2002).
55. Beldi, E. et al. The revisited genome of *Pseudomonas putida* KT2440 enlightens its value as a robust metabolic chassis. *Environ. Microbiol.* **18**, 3403–3424 (2016).
56. Koendjibarie, J. G., van Kranenburg, R. & Kengen, S. W. M. The PEP-pyruvate-oxaloacetate node: variation at the heart of metabolism. *FEMS Microbiol. Rev.* **45**, fuaa061 (2021).
57. Roca, A., Rodríguez-Hervá, J. J. & Ramos, J. L. Redundancy of enzymes for formaldehyde detoxification in *Pseudomonas putida*. *J. Bacteriol.* **191**, 3367–3374 (2009).
58. Ramos, J. L. et al. Mechanisms of solvent tolerance in gram-negative bacteria. *Annu. Rev. Microbiol.* **56**, 743–768 (2002).
59. Basler, G., Thompson, M., Tullman-Ercek, D. & Keasling, J. A *Pseudomonas putida* efflux pump acts on short-chain alcohols. *Biotechnol. Biofuels* **11**, 136 (2018).
60. Mendonça, C. M. et al. Hierarchical routing in carbon metabolism favors iron-scavenging strategy in iron-deficient soil *Pseudomonas* species. *Proc. Natl. Acad. Sci. USA* **117**, 32358–32369 (2020).
61. Wilkes, R. A. et al. Complex regulation in a *Comamonas* platform for diverse aromatic carbon metabolism. *Nat. Chem. Biol.* 1–12 <https://doi.org/10.1038/s41589-022-01237-7> (2023).
62. Tiffert, T., García-Sancho, J. & Lew, V. L. Irreversible ATP depletion caused by low concentrations of formaldehyde and of calcium-chelator esters in intact human red cells. *Biochim. et. Biophys. Acta* **773**, 143–156 (1984).
63. Javidpour, P. et al. Biochemical and structural studies of NADH-dependent FabG used to increase the bacterial production of fatty acids under anaerobic conditions. *Appl. Environ. Microbiol.* **80**, 497–505 (2014).
64. Xu, Z. et al. Enhancement of polyhydroxyalkanoate production by co-feeding lignin derivatives with glycerol in *Pseudomonas putida* KT2440. *Biotechnol. Biofuels* **14**, 11 (2021).
65. Yang, H. et al. Engineering *streptomyces albulus* to enhance ε-poly-L-lysine production by introducing a polyphosphate kinase-mediated ATP regeneration system. *Microb. Cell Fact.* **22**, 51 (2023).
66. Harayama, S. & Rekik, M. The meta cleavage operon of TOL degradative plasmid pWWO comprises 13 genes. *Mol. Gen. Genet.* **221**, 113–120 (1990).
67. Kamimura, N. & Masai, E. The protocatechuate 4,5-cleavage pathway: overview and new findings. in *Biodegradative Bacteria: How Bacteria Degrade, Survive, Adapt, and Evolve* (eds Nojiri, H., Tsuda, M., Fukuda, M. & Kamagata, Y.) 207–226 (Springer, 2014).
68. Varman, A. M. et al. Decoding how a soil bacterium extracts building blocks and metabolic energy from ligninolysis provides road map for lignin valorization. *Proc. Natl. Acad. Sci. USA* **113**, E5802–E5811 (2016).
69. Borrero-de Acuña, J. M. et al. Channelling carbon flux through the meta-cleavage route for improved poly(3-hydroxyalkanoate) production from benzoate and lignin-based aromatics in *Pseudomonas putida* H. *Micro. Biotechnol.* **14**, 2385–2402 (2021).
70. Salvachúa, D., M. Karp, E., Nimlos, T. & R. Vardon, C. D. & T. Beckham, G. Towards lignin consolidated bioprocessing: simultaneous lignin depolymerization and product generation by bacteria. *Green. Chem.* **17**, 4951–4967 (2015).
71. Karp, E. et al. Quantification of acidic compounds in complex biomass-derived streams. *Green. Chem.* **18**, 4750–4760 (2016).
72. Cetnar, D. P. & Salis, H. M. Systematic quantification of sequence and structural determinants controlling mRNA stability in bacterial operons. *ACS Synth. Biol.* **10**, 318–332 (2021).
73. Schmidt, M. et al. Maximizing heterologous expression of engineered Type I polyketide synthases: investigating codon optimization strategies. *ACS Synth. Biol.* **12**, 3366–3380 (2023).

74. Elmore, J. R. et al. High-throughput genetic engineering of nonmodel and undomesticated bacteria via iterative site-specific genome integration. *Sci. Adv.* **9**, eade1285 (2023).
75. Elsayyid, M., Taris, J. E. & Yu, Y. Simple in-cell processing enables deep proteome analysis of low-input *caenorhabditis elegans*. *Anal. Chem.* **97**, 9159–9167 (2025).
76. Martin, K. R. et al. Development of an efficient, effective, and economical technology for proteome analysis. *Cell Rep. Methods* **4**, 100796 (2024).
77. Reilly, L. et al. A fully automated FAIMS-DIA mass spectrometry-based proteomic pipeline. *Cell Rep. Methods* **3**, 100593 (2023).
78. Bruderer, R. et al. Extending the limits of quantitative proteome profiling with data-independent acquisition and application to acetaminophen-treated three-dimensional liver microtissues. *Mol. Cell Proteom.* **14**, 1400–1410 (2015).
79. Tyanova, S. et al. The Perseus computational platform for comprehensive analysis of (prote)omics data. *Nat. Methods* **13**, 731–740 (2016).
80. Bennett, B. D., Yuan, J., Kimball, E. H. & Rabinowitz, J. D. Absolute quantitation of intracellular metabolite concentrations by an isotope ratio-based approach. *Nat. Protoc.* **3**, 1299–1311 (2008).
81. Aristilde, L. et al. Glyphosate-induced specific and widespread perturbations in the metabolome of soil *pseudomonas* species. *Front. Environ. Sci.* **5**, <https://doi.org/10.3389/fenvs.2017.00034> (2017).
82. Mendonca, C. M., Zhang, L., Waldbauer, J. R. & Aristilde, L. Disproportionate carbon dioxide efflux in bacterial metabolic pathways for different organic substrates leads to variable contribution to carbon-use efficiency. *Environ. Sci. Technol.* <https://doi.org/10.1021/acs.est.4c01328> (2024).
83. Munger, J. et al. Systems-level metabolic flux profiling identifies fatty acid synthesis as a target for antiviral therapy. *Nat. Biotechnol.* **26**, 1179–1186 (2008).
84. Park, J. O. et al. Metabolite concentrations, fluxes and free energies imply efficient enzyme usage. *Nat. Chem. Biol.* **12**, 482–489 (2016).
85. Pisithkul, T. et al. Metabolic remodeling during biofilm development of *Bacillus subtilis*. *mBio* **10**, <https://doi.org/10.1128/mbio.00623-19> (2019).
86. Clasquin, M. F., Melamud, E. & Rabinowitz, J. D. LC-MS data processing with maven: a metabolomic analysis and visualization engine. *Curr. Protoc. Bioinform.* <https://doi.org/10.1002/0471250953.bi1411s37> Unit14.11 (2012).
87. Millard, P. et al. IsoCor: isotope correction for high-resolution MS labeling experiments. *Bioinformatics* **35**, 4484–4487 (2019).
88. Nogales, J. et al. High-quality genome-scale metabolic modelling of *Pseudomonas putida* highlights its broad metabolic capabilities. *Environ. Microbiol.* **22**, 255–269 (2020).
89. Young, J. D. INCA: a computational platform for isotopically non-stationary metabolic flux analysis. *Bioinformatics* **30**, 1333–1335 (2014).
90. Ebrahim, A., Lerman, J. A., Palsson, B. O. & Hyduke, D. R. COBRAPy: COnstraints-based reconstruction and analysis for python. *BMC Syst. Biol.* **7**, 74 (2013).
91. Volke, D. C., Olavarria, K. & Nikel, P. I. Cofactor specificity of glucose-6-phosphate dehydrogenase isozymes in *Pseudomonas putida*: Reveals a general principle underlying glycolytic strategies in bacteria. *mSystems* **6**, <https://doi.org/10.1128/msystems.00014-21> (2021).
92. Tanaka, N., Kusakabe, Y., Ito, K., Yoshimoto, T. & Nakamura, K. T. Crystal structure of formaldehyde dehydrogenase from *Pseudomonas putida*: the structural origin of the tightly bound cofactor in nicotinoprotein dehydrogenases. *J. Mol. Biol.* **324**, 519–533 (2002).
93. Zobel, S., Kuepper, J., Ebert, B., Wierckx, N. & Blank, L. M. Metabolic response of *Pseudomonas putida* to increased NADH regeneration rates. *Eng. Life Sci.* **17**, 47–57 (2017).

Acknowledgements

This material is based upon work supported by the U.S. Department of Energy (DOE), Office of Science, Office of Biological and Environmental Research, Genomic Science Program under Award Number DE-SC0022181. This work was authored in part by the National Renewable Energy Laboratory, operated by Alliance for Sustainable Energy, LLC, for the U.S. DOE under Contract No. DE-AC36-08GO28308. We thank Jeffrey Czajka at Pacific Northwest National Laboratory and Shawn Xiao at Washington University in St. Louis for helpful advice during ^{13}C -fluxomics modeling using the INCA software. The views expressed in the article do not necessarily represent the views of the DOE or the U.S. Government. The U.S. Government retains, and the publisher, by accepting the article for publication, acknowledges that the U.S. Government retains a nonexclusive, paid-up, irrevocable, worldwide license to publish or reproduce the published form of this work, or allow others to do so, for U.S. Government purposes.

Author contributions

N.Z., R.A.W., X.C., K.P.T., J.A.B., and Y.Y. performed research. G.T.B. and A.Z.W. provided resources. N.Z. and L.A. designed research, analyzed data, and wrote manuscript. L.A. supervised research.

Competing interests

The authors declare no competing interests.

Additional information

Supplementary information The online version contains supplementary material available at <https://doi.org/10.1038/s42003-025-08723-3>.

Correspondence and requests for materials should be addressed to Ludmilla Aristilde.

Peer review information *Communications Biology* thanks Yinjie Tang, Suresh Sudarsan and the other anonymous reviewer(s) for their contribution to the peer review of this work. Primary Handling Editors: Haichun Gao and David Favero. A peer review file is available.

Reprints and permissions information is available at <http://www.nature.com/reprints>

Publisher's note Springer Nature remains neutral with regard to jurisdictional claims in published maps and institutional affiliations.

Open Access This article is licensed under a Creative Commons Attribution-NonCommercial-NoDerivatives 4.0 International License, which permits any non-commercial use, sharing, distribution and reproduction in any medium or format, as long as you give appropriate credit to the original author(s) and the source, provide a link to the Creative Commons licence, and indicate if you modified the licensed material. You do not have permission under this licence to share adapted material derived from this article or parts of it. The images or other third party material in this article are included in the article's Creative Commons licence, unless indicated otherwise in a credit line to the material. If material is not included in the article's Creative Commons licence and your intended use is not permitted by statutory regulation or exceeds the permitted use, you will need to obtain permission directly from the copyright holder. To view a copy of this licence, visit <http://creativecommons.org/licenses/by-nc-nd/4.0/>.

© The Author(s) 2025